

# Frontal Slice Approaches for Tensor Linear Systems

Hengrui Luo<sup>13</sup>, Anna Ma<sup>2</sup>

<sup>1</sup> *Department of Statistics, Rice University, Houston, 77005, USA*

<sup>2</sup> *Department of Mathematics, University of California, Irvine, 92617, USA*

<sup>3</sup> *Computational Research Division, Lawrence Berkeley National Laboratory, Berkeley, 94701, USA*

---

**Abstract.** Inspired by the row and column action methods for solving large-scale linear systems, in this work, we explore the use of frontal slices for solving tensor linear systems. In particular, this paper presents a novel approach for using frontal slices of a tensor  $\mathcal{A}$  to solve tensor linear systems  $\mathcal{A} * \mathcal{X} = \mathcal{B}$  where  $*$  denotes the t-product. In addition, we consider variations of this method, including cyclic, block, and randomized approaches, each designed to optimize performance in different operational contexts. Our primary contribution lies in the development and convergence analysis of these methods. Experimental results on synthetically generated and real-world data, including applications such as image and video deblurring, demonstrate the efficacy of our proposed approaches and validate our theoretical findings.

**AMS subject classifications:** 15A69, 15A72, 65F10

**Key words:** tensor linear systems, t-product, iterative methods, tensor sketching

---

## 1. Introduction

In the realm of contemporary data science, the availability of multi-dimensional data, commonly referred to as tensors, has catalyzed transformative advances across diverse domains such as machine learning [8, 41], neuroimaging [35], recommendation systems [6] and signal processing [7, 39, 42]. Tensors, which extend beyond the simpler constructs of matrices, encapsulate higher-order interactions within data that matrices alone cannot. While potentially offering a more comprehensive framework for analysis and predictive modeling [7, 24], tensors come with complexity and high dimensionality, which introduce escalated computational costs and demanding storage requirements, particularly in large-scale and high-fidelity compressible datasets [1, 22].

In this work, we are interested in solving large-scale consistent tensor multi-linear systems of the form

$$\mathcal{A} * \mathcal{X} = \mathcal{B}, \tag{1.1}$$

where  $\mathcal{A} \in \mathbb{R}^{n_1 \times n_2 \times n}$ ,  $\mathcal{X} \in \mathbb{R}^{n_2 \times n_3 \times n}$ ,  $\mathcal{B} \in \mathbb{R}^{n_1 \times n_3 \times n}$ , and  $*$  denotes the tensor product, known as the *t-product* [23]. Direct solvers for solving tensor linear systems induce high computational complexity [4, 5, 18]. As an alternative, iterative algorithms for such approximating solutions to (1.1) have been previously studied [10, 25, 27] and have applications for image and video deblurring, regression, dictionary learning, and facial recognition [12, 19, 41].

The t-product can be viewed as a generalization of the matrix-vector product. In particular, when  $n = 1$  and  $n_3 = 1$ , the t-product simplifies to the matrix-vector product. In the matrix-data setting, row and column iterative methods have been proposed to solve large-scale linear systems of equations

$$\mathbf{A}\mathbf{x} = \mathbf{b}, \quad (1.2)$$

where  $\mathbf{A} \in \mathbb{R}^{n_1 \times n_2}$ ,  $\mathbf{b} \in \mathbb{R}^{n_1 \times 1}$  are given and  $\mathbf{x} \in \mathbb{R}^{n_2 \times 1}$  is unknown. When  $n_1$  and  $n_2$  are very large, solving the linear system directly (e.g., by computing the pseudo-inverse) quickly becomes impractical. In other large-scale settings, one may not even be able to load all entries but only a few rows or columns of the matrix  $\mathbf{A}$  at a time. In such settings, stochastic iterative methods with low memory footprints, such as the Randomized Kaczmarz or Randomized Gauss-Seidel (RGS) algorithms, can be used to solve (1.2). The relationship between these two methods, one using rows of the matrix and the other using columns of the matrix, has been studied in previous works [37]. Such row and column action methods solving linear systems have been further generalized to a framework known as *sketch-and-project* [8, 16, 17, 39, 40].

Sketching simplifies computations by solving a sub-system as a proxy to the original system while preserving the data’s intrinsic characteristics, thereby addressing the practical limitations of direct manipulation due to size or complexity [39, 40, 45], which proves essential in scenarios where handling full datasets is impractical. A primary advantage of sketching is the enhancement of computational efficiency. In tensor operations such as multiplications or factorizations, multiplication complexity (and so is the solving complexity) can increase exponentially with the sizes of the tensor mode (See Proposition 1). Sketching techniques reduce the effective dimensionality of the tensor system, which in turn accelerates computations and diminishes the burden on memory resources. This improvement is vital in real-time processing applications like video processing [24, 28, 33], where swift and efficient processing is crucial.

Previous works considered sketches under the t-product. For example, [36] propose the tensor Randomized Kaczmarz Algorithm, where “row-slices” (instead of matrix rows), corresponding to row sketching, are utilized at every iteration (TRK). Other works [39] have considered solving tensor multi-linear systems using a general sketch-and-project framework. The work by [36] encapsulates the TRK algorithm for the sketch-and-project regime for tensor systems.

Although the tensorized versions of RK and the sketch-and-project framework have been proposed and studied, they do not capture settings unique to the tensor landscape by nature of being extensions of matrix-based algorithms. In this work, we propose a suite of *frontal-slice-based* iterative methods for approximating the solution to tensor

linear systems. Our main contributions include:

1. Variations (cyclic, block, and randomized) of methods that utilize frontal slices to approximation solutions to multi-linear tensor systems under the t-product
2. Convergence and computational complexity analysis for the cyclic frontal slice-based method and its variants.
3. Empirical comparison of our proposed methods to other tensor sketching methods and real-world image and video data.

All the aforementioned algorithms are indicative of a broader trend in tensor computation, where methods are adapted or developed to exploit the multi-dimensional structure of tensors. By focusing on individual slices, these algorithms offer a more manageable and potentially more efficient approach to solving tensor-based problems compared to methods that must consider the entire tensor at each step.

**Organization.** The rest of the paper is organized as follows: Section 2 presents related work and background on the tensor t-product. Section 3 covers our main algorithms, including the classic gradient descent and our proposed algorithms, which balance storage and computational complexities. Section 4 provides algorithm convergence guarantees. Section 5 uses synthetic and real-world experiments to validate our results empirically. Lastly, Section 6 discusses our findings and points to some interesting future works.

## 2. Background

This section reviews related works and presents necessary background information regarding the tensor t-product.

**Notation.** Calligraphic letters are reserved for tensors, capital letters for matrices, and lowercase letters for vectors and indices. We adopt MATLAB notation to reference elements or slices of a tensor, where a “slice” refers to a sub-tensor in which one index is fixed. For example,  $\mathcal{A}_{i::}$  denotes the  $i$ -th row slice of dimension  $1 \times n_2 \times n$  of  $\mathcal{A}$  and  $a_{ijk} \in \mathbb{R}$  denotes the  $(i, j, k)$ -th element of  $\mathcal{A}$ . Since frontal slices will be used frequently, we shorten the notation of frontal slices to  $\mathcal{A}_k$ . Figure 1 presents a visual representation of the row and frontal slices of a tensor. We assume that  $\mathcal{A}$  and  $\mathcal{B}$  in (1.1) are known, and our goal is to approximate  $\mathcal{X}$ , where  $\mathcal{X}$  is the unique, exact solution to (1.1).

### 2.1. The Tensor t-product

The tensor t-product [23] is an operation in tensor algebra motivated to generalize the concept of matrix multiplication to tensors. While the t-product can be further generalized to higher order tensors and to use other orthogonal transforms [21, 43], here, we present the original form of the t-product, using third-order tensors associated with

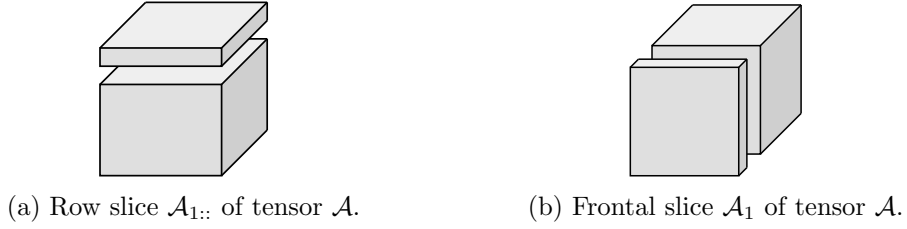


Figure 1: The first row slice  $\mathcal{A}_{1,:}$  and frontal slice  $\mathcal{A}_1$  of  $\mathcal{A}$ .

the Fourier Transform. Readers who are well-acquainted with the t-product may skip this section and proceed to Section 3. Before defining the t-product, we first introduce two tensor operations.

**Definition 2.1.** (*Tensor operations, [23]*) For  $\mathcal{A} \in \mathbb{R}^{n_1 \times n_2 \times n}$ , let  $\text{unfold}(\mathcal{A})$  denote the unfolded tensor

$$\text{unfold}(\mathcal{A}) = \begin{pmatrix} A_1 \\ A_2 \\ \vdots \\ A_n \end{pmatrix} \in \mathbb{R}^{n_1 n_2 \times n}.$$

The inverse of the unfolding operation is denoted  $\text{fold}(\cdot)$  and is such that  $\text{fold}(\text{unfold}(\mathcal{A})) = \mathcal{A}$ . Let  $\text{bcirc}(\mathcal{A})$  denote the block-circulant matrix

$$\text{bcirc}(\mathcal{A}) = \begin{pmatrix} A_1 & A_n & A_{n-1} & \dots & A_2 \\ A_2 & A_1 & A_n & \dots & A_3 \\ \vdots & \vdots & \vdots & \ddots & \vdots \\ A_n & A_{n-1} & A_{n-2} & \dots & A_1 \end{pmatrix} \in \mathbb{R}^{n_1 n_2 \times n_1 n_2}. \quad (2.1)$$

**Definition 2.2.** (*Tensor product (t-product), [23]*) Given  $\mathcal{A} \in \mathbb{R}^{n_1 \times n_2 \times n}$  and  $\mathcal{X} \in \mathbb{R}^{n_2 \times n_3 \times n}$ , the t-product is defined as

$$\mathcal{A} * \mathcal{X} = \text{fold}(\text{bcirc}(\mathcal{A}) \text{unfold}(\mathcal{X})) \in \mathbb{R}^{n_1 \times n_3 \times n}.$$

Since circulant matrices are diagonalizable by the Fourier Transform, computationally, the t-product can be efficiently performed by computing the Discrete Fourier Transform (DFT) along each tensor's third dimension, multiplying the corresponding frontal slices in the Fourier domain and then applying the Inverse Discrete Fourier Transform (IDFT) to the product. It should be noted that because this transformation is applied along the third mode of the tensor, it requires all  $n$  frontal slices. So if only one frontal slice of  $\mathcal{A}$  in (1.1) is given at a time, the  $\text{bcirc}(\mathcal{A})$  is not complete and its diagonalization is not immediately computable.

**Data perspectives.** Unlike matrix-vector products, data tensors are flexible that they admits a variety of tensor products. Before we move on, let us briefly compare the t-product to two other popular tensor products: the Kronecker product and the Khatri-Rao product. Practitioners usually treat matrices as data whose rows are samples and columns are features. In the tensor data setting [3, 33], data tensors use additional dimensions (e.g., frontal dimension) to represent multiple instances of sample feature sets. One concrete example is video tensor  $\mathcal{A}$ , where frontal slices  $\mathcal{A}_i$  represent different pixel-by-pixel frames.

The Kronecker product between two matrices  $\mathbf{A}$  and  $\mathbf{B}$  results in a new matrix where each scalar element  $a_{ij}$  of matrix  $\mathbf{A}$  is multiplied by the entire matrix  $\mathbf{B}$ . This can be extended to tensors. In particular, the Kronecker product between two tensors  $\mathcal{A}$  and  $\mathcal{B}$  is defined as a larger tensor  $\mathcal{C}$  such that each element  $a_{ijk}$  of  $\mathcal{A}$  is multiplied by the entire tensor  $\mathcal{B}$ . Geometrically, this represents a multidimensional scaling where every element of  $\mathcal{B}$  is scaled by corresponding elements of  $\mathcal{A}$ , creating a much larger tensor that encodes all combinations of the elements from  $\mathcal{A}$  and  $\mathcal{B}$ .

The Khatri-Rao product [29, 42] is a “column-wise” Kronecker product. For matrices, it can be thought of as taking the Kronecker product of corresponding columns from two matrices. For two tensors  $\mathcal{A}$  and  $\mathcal{B}$  with equal numbers of slices along a dimension, the Khatri-Rao product is formed by the column-wise Kronecker product of corresponding slices from  $\mathcal{A}$  and  $\mathcal{B}$  along that shared dimension. Geometrically, this can be viewed as combining features from two different matrices (or tensors) at a more granular (coarser but more regulated) level than the Kronecker product. If we imagine each column of the matrix (or slice of the tensor) as a feature, the Khatri-Rao product combines these features in a way that every feature in one vector (tensor slice) is paired with every feature in the corresponding column of the other matrix (tensor slice), producing a detailed and granular new feature space. It preserves more structure compared to the Kronecker product and is often used in scenarios where the interaction between corresponding features (columns) is crucial.

The t-product [23] allows tensors to interact across slices in a more complex way, using a chosen transform, in our case the Fourier transform. In contrast to the Kronecker and Khatri-Rao products, the t-product utilizes a convolutional operation along the frontal dimension of the tensors  $\mathcal{A}$  and  $\mathcal{B}$ . If we imagine each column of the matrix (or frontal slice of the tensor) as a feature, the t-product combines every feature in one vector (or tensor) paired with every feature in the corresponding column of the other matrix (or slice of the other tensor) by taking product in the Fourier domain (hence taking convolution in the original domain) to form a new feature space. This convolution-like process essentially mixes the frontal slices of the tensors based on their relative positions, integrating them into a new tensor whose slices are combinations of the original slices manipulated through the circulant structure. However, when the frontal dimension is of size 1, there is no convolution, reducing the t-product to our usual matrix product.

As the need for higher-dimensional data representations grows in fields such as computer vision, signal processing, and machine learning, exploring and developing operations that extend the t-product to higher-order tensors becomes essential. These

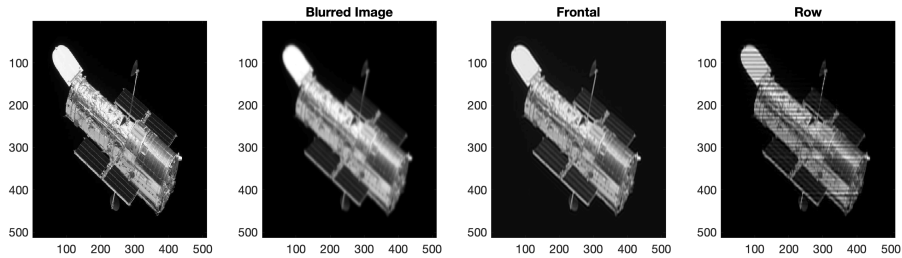


Figure 2: The original  $512 \times 512$  pixel image of the Hubble Space Telescope [https://github.com/jnagy1/IRtools/blob/master/Extra/test\\_data/HSTgray.jpg](https://github.com/jnagy1/IRtools/blob/master/Extra/test_data/HSTgray.jpg), its Gaussian blurred version and the frontal sketching (Algorithm 3.2) deblurred version. We defer the details of this deblurring experiment to Section 5.

higher-order tensors (order greater than three) can represent more complex data structures, capturing additional modes of variability. The higher-order t-product can be defined recursively, as suggested by [38]. For instance, consider a fourth-order tensor  $\mathcal{A} \in \mathbb{R}^{n \times m \times p \times q}$ . The t-product for fourth-order tensors can be constructed by treating  $\mathcal{A}$  as a tensor in  $\mathbb{R}^{n \times n \times (pq)}$ , where the last two modes are merged into a single mode, and then applying the t-product recursively.

In extending linear systems sketching to the tensor setting, there are multiple options for operating on tensors such as using the t-product [26, 46]. The t-product has been of particular interest due to its natural extension of many desirable linear algebraic properties and definitions.

In this work, we focus on t-product for tensors of 3 modes due to its wide applicability. The tensor t-product generalizes linear transformations and matrix multiplication to higher dimensions, facilitating the development of algorithms that can manipulate multi-dimensional arrays efficiently. The transformation step typically uses fast transform methods, such as the Fast Fourier Transform (FFT), which are computationally efficient and widely supported in various software and hardware implementations, enhancing the practicality of using tensor t-products in large-scale applications. Unlike matrices, tensors can encapsulate data with multiple dimensions without losing inherent multi-way relationships, making tensor operations particularly suitable for complex data structures found in modern applications like signal processing and machine learning. In Figure 2, we show the frontal sketching effectively deblurs images by treating them as third-order tensors. The sketching method not only preserves spatial and temporal correlations, ensuring each update incorporates information from all slices, but also provides a significantly clearer image, which demonstrates the power of tensor-based techniques in image deblurring. Before presenting our algorithmic approach, we first present additional useful definitions for this work.

**Definition 2.3.** (*Identity tensor, [23]*) The identity tensor  $\mathcal{I} \in \mathbb{R}^{n_1 \times n_1 \times n}$  is defined as a tensor whose first frontal slice is the identity matrix and is zero elsewhere.

**Definition 2.4.** (*Transpose, [23]*) Let  $\mathcal{A} \in \mathbb{R}^{n_1 \times n_2 \times n}$  then  $\mathcal{A}^T$  is obtained by transposing

each frontal slice and reversing the order of slices 2 to  $n$ .

Note that the identity tensor is defined such that, under the t-product,  $\mathcal{A} * \mathcal{I} = \mathcal{A}$  and  $\mathcal{I} * \mathcal{A} = \mathcal{A}$ , for appropriately sized tensors. Furthermore, the transpose is defined such that not only does  $(\mathcal{A}^T)^T = \mathcal{A}$  hold, it also holds that under the t-product  $(\mathcal{A} * \mathcal{B})^T = \mathcal{B}^T * \mathcal{A}^T$ , which is not generally valid for other tensor products.

**Definition 2.5.** (*Tensor Norms, [11]*) We define the squared Frobenius norm of  $\mathcal{A} \in \mathbb{R}^{n_1 \times n_2 \times n}$  as

$$\|\mathcal{A}\|_F^2 = \sum_{i=1}^{n_1} \sum_{j=1}^{n_2} \sum_{k=1}^n a_{ijk}^2, \quad (2.2)$$

where  $a_{ijk}$  is the  $(i, j, k)$ -th entry of  $\mathcal{A}$ . The operator norm of  $\mathcal{A}$  is defined as

$$\|\mathcal{A}\|_{op} := \sup_{\|\mathcal{X}\|_F=1} \|\mathcal{A} * \mathcal{X}\|_F = \|\text{bcirc}(\mathcal{A})\|_2, \quad (2.3)$$

where  $\|\cdot\|_2$  denotes the usual matrix 2-norm for the block circulant matrix.

**Remark 1.** by Definition 2.5, it holds that

$$\|\mathcal{A} * \mathcal{X}\|_F \leq \|\mathcal{A}\|_{op} \|\mathcal{X}\|_F,$$

for appropriately sized tensors  $\mathcal{A}$  and  $\mathcal{X}$ .

## 2.2. Related Works

Major interest from the statistics community focuses on extending the tensor regression problem, whose solution depends on (1.1). For example, [32] high-dimensional quantile tensor regression utilizes convex decomposable regularizers to approximate the solution to (1.1) using the incremental proximal gradient method, which bears much worse complexity than gradient descent [2]. Another generalization by [20] incorporates an  $L_1$  norm penalization term and solves (1.1) using a block coordinate descent algorithm and each block of coordinates [13]. While the convergence rates of the coordinate descent algorithm for tensor variant is unknown, the nested optimization introduces a higher complexity than the gradient descent. For generalized tensor models [15], the optimization problem based on (1.1) can be even more expensive, although it still depends on (1.1) in a vectorized form. The scalability of the gradient descent algorithm needs to be investigated beyond the small size (i.e., each mode of the tensor is usually smaller than 100 in these papers' examples) when the common practice of sketch-and-project is in the play.

Previous works have considered the application of iterative methods to solve (1.1). In [36], the authors propose a tensor-based Kaczmarz method. The proposed method was shown to be a special case of the more general tensor sketch-and-project (TSP) method, which was proposed and studied by [44], based on the matrix sketch-and-project framework of [17]. In the TSP method, a sketch tensor  $\mathcal{S} \in \mathbb{R}^{k \times n_1 \times n}$  is multiplied with

$\mathcal{A}$  to obtain its sketch, and then an objective is minimized subject to the sketch itself, i.e., the iterates  $\mathcal{X}(t+1)$  are approximated by solving the minimization problem

$$\mathcal{X}(t+1) = \operatorname{argmin}_{\mathcal{X}} \|\mathcal{X} - \mathcal{X}(t)\|_F^2 \text{ s.t. } \mathcal{S}^T * \mathcal{A} * \mathcal{X} = \mathcal{S}^T * \mathcal{B}. \quad (2.4)$$

The closed-form solution of this minimization problem is written as:

$$\mathcal{X}(t+1) = \mathcal{X}(t) + \mathcal{A}^T * \mathcal{S} * (\mathcal{S}^T * \mathcal{A} * \mathcal{A}^T * \mathcal{S})^\dagger * \mathcal{S} * (\mathcal{B} - \mathcal{A} * \mathcal{X}(t)), \quad (2.5)$$

where the notation  $(\cdot)^\dagger$  denotes the Moore-Penrose pseudoinverse defined in [44]. Choosing  $k=1$  and  $\mathcal{S} \in \mathbb{R}^{1 \times n_2 \times n}$  where, for a fixed index  $i \in [n_2]$ ,  $\mathcal{S}_{1ij} = 1$  for all  $j \in [n]$  and zero otherwise, creates a ‘‘row sketch’’ of  $\mathcal{A}$ , i.e.,  $\mathcal{S}_i * \mathcal{A} = \mathcal{A}_{i::}$ . In this setting, single-row slices of the data tensor  $\mathcal{A}$  and row slices of  $\mathcal{B}$  are utilized a time, and the TSP method recovers the TRK algorithm of [36]. Similarly, a column-slice-based method, which only uses single column slices at a time, can be derived using the TSP method. Unfortunately, for sketches  $\mathcal{S}_i$  to obtain frontal slices  $\tilde{\mathcal{A}}_i$ , where  $\tilde{\mathcal{A}}_i \in \mathbb{R}^{n_1 \times n_2 \times n}$  denotes a tensor with  $\mathcal{A}_i$  in the  $i$ -th frontal slice and zero elsewhere,  $\mathcal{S}_i$  would need to depend on  $\mathcal{A}$ , using all frontal slices of  $\mathcal{A}$ . This may not be feasible if only frontal slice-wise information is accessible at a time, thus restricting the use of sketch and project methods to reduce computational overhead.

While column-slice and row-slice sketching are well-studied, the sketching along the frontal dimension, which differentiates tensors from matrices, remains unexplored. In this work, we consider a unique setting to solving tensor systems via frontal-slice sampling. While row and column sketching fall under the sketch-and-project framework [8, 39, 47], the approaches proposed here does not.

### 3. The Frontal Slice Descent Algorithm

We approach the design of an iterative method that uses frontal slices of  $\mathcal{A}$  via a decomposition of the gradient descent iterates applied to the least squares objective. In doing so, we derive two variations of the proposed method, which we refer to as the Frontal Slice Descent (FSD) method. To that end, let  $\mathcal{F}(\mathcal{X}) = \frac{1}{2} \|\mathcal{A} * \mathcal{X} - \mathcal{B}\|^2$  denote the least squares objective function for the system (1.1), then the gradient can be written as  $\nabla \mathcal{F} = \mathcal{A}^T * (\mathcal{A} * \mathcal{X} - \mathcal{B})$ . Thus, applying gradient descent to approximate solutions to (1.1) produces the iterates

$$\mathcal{X}(t+1) = \mathcal{X}(t) + \alpha \mathcal{A}^T * (\mathcal{B} - \mathcal{A} * \mathcal{X}(t)), \quad (3.1)$$

where  $\alpha \in \mathbb{R}^+$  is assumed to be a fixed learning rate for simplicity. Algorithm 3.1 presents pseudo-code for this approach. In the algorithm, we initial residual tensor  $\mathcal{R} = \mathcal{B} - \mathcal{A} * \mathcal{X}$  is set to  $\mathcal{B}$  and the initial approximation of  $\mathcal{X}$  is set to zero. Then, iterative updates to  $\mathcal{R}$  and  $\mathcal{X}$  are performed. The update for  $\mathcal{R}$  involves subtracting the product of  $\mathcal{A}$  and  $\mathcal{X}$ , representing the difference between the current estimate and the measurements. The update for  $\mathcal{X}$  involves a step in the direction of the gradient of the residual, scaled by a



learning rate  $\alpha$ . This is akin to classical gradient descent but adapted for tensors.

The use of the full gradient (3.4) in each step, suggests that this algorithm is designed for scenarios where computing the full gradient is feasible. This may not be the case for very large-scale problems, where only some of  $\mathcal{A}$  is available at a time due to (e.g., memory) constraints. This algorithm is the primary variant for its application in multi-dimensional data contexts, offering a way to harness the structure and relationships inherent in tensor data. For practitioners, it's important to consider the computational cost and the convergence properties of this method, particularly in relation to the size and complexity of the data tensors involved.

Algorithm 3.1 can be computationally expensive, especially for large tensors. We propose a novel algorithm that uses one frontal slice per iteration to remedy the per-iteration information needed from  $\mathcal{A}$ . This adaptation presents an innovative way to exploit the multi-dimensional nature of tensors, offering a feasible and efficient approach to tensor-based optimization problems using only frontal slices of  $\mathcal{A}$  per iteration.

---

**Algorithm 3.1** Gradient descent for t-product least squares problem (1.1).

---

**Input:** data matrix  $\mathcal{A}$ , measurements  $\mathcal{B}$ , learning rate  $\alpha$

**Initialize**  $\mathcal{R}(0) = \mathcal{B}$ ,  $\mathcal{X}(0) = \mathbf{0}$ ,  $t = 0$

**while** stopping criteria not satisfied **do**

$\mathcal{R}(t + 1) = \mathcal{B} - \mathcal{A} * \mathcal{X}(t)$

    ▷ Residual at iteration  $t + 1$

$\mathcal{X}(t + 1) = \mathcal{X}(t) + \alpha \mathcal{A}^T * \mathcal{R}(t + 1)$

    ▷ Gradient step

$t = t + 1$

---

### 3.1. Using Frontal Slices

The t-product gradient descent algorithm (Algorithm 3.1) geometrically represents an iterative process of aligning tensor slices through dynamic convolutional interactions. The circular convolution integrates spatial relationships between slices, and the transpose operation ensures that adjustments are made coherently to align the tensors optimally.

In the  $t$ -th iteration, the algorithm works iteratively to align the tensor  $\mathcal{X}(t)$  with  $\mathcal{B}$  in the t-product sense. Each iteration refines this alignment through the convolutional interactions represented by the t-product. The circular convolution  $\mathcal{A} * \mathcal{X}(t)$  integrates adjacent slice information, and the algorithm adjusts  $\mathcal{X}(t)$  into  $\mathcal{X}(t + 1) = \mathcal{X}(t) + \alpha \mathcal{A}^T * \mathcal{R}(t + 1)$  to account for misalignments across adjacent slices in  $\mathcal{B}$ . The gradient  $\mathcal{A}^T * \mathcal{R}(t + 1)$  points in the direction of the steepest descent, where each iteration accounts for the convolutional effect of adjacent slices, hence maintaining the geometric integrity of the circular convolution relationship. Given appropriate step sizes  $\alpha$ , the method iteratively reduces the error until it converges to the solution.

The proposed method approximates the solution to  $\mathcal{A} * \mathcal{X} = \mathcal{B}$  by iteratively updating the tensor  $\mathcal{X}$  based on the current residual  $\mathcal{R}$  and the selected slice of  $\mathcal{A}$ . Using a single slice for each update, as opposed to the full tensor can significantly reduce communication cost (needing only  $\mathcal{A}_i$  with  $n_1 n_2$  entries instead of all  $n_1 n_2 n$  elements from  $\mathcal{A}$ ), making

these algorithms suitable for large-scale tensor problems. The remainder of this section focuses on the derivation of our method and the residual approximation.

Instead of using all frontal slices in each iteration, our goal is to approximate  $\nabla\mathcal{F}$  using only one frontal slice at a time. Although  $\mathcal{F}$  cannot be additively decomposed with respect to frontal slices, we can still design methods that use a frontal slice at a time. Define  $\tilde{\mathcal{A}}_i \in \mathbb{R}^{n_1 \times n_2 \times n}$ , such that the  $i$ -th frontal slice of  $\tilde{\mathcal{A}}_i$  is the  $i$ -th frontal slice of  $\mathcal{A}$  and  $\tilde{\mathcal{A}}_i$  is zero elsewhere. Then,  $\mathcal{A}$  can be written as a sum of its frontal slices  $\mathcal{A} = \sum_{i=1}^n \tilde{\mathcal{A}}_i$ . Thus, the gradient can be written as

$$\nabla\mathcal{F}(\mathcal{X}) = \sum_{i=1}^n \tilde{\mathcal{A}}_i^T * (\mathcal{B} - \mathcal{A} * \mathcal{X}).$$

Unfortunately, the residual,  $\mathcal{B} - \mathcal{A} * \mathcal{X}$  cannot be computed without all frontal slices. However, it can be approximated. Suppose that at iteration  $i(t)$ , frontal slice  $\mathcal{A}_{i(t)}$  is given (e.g.,  $i(t) = i(t-n+1)$  represents cyclic indexing), then we propose to approximate  $\nabla\mathcal{F}$  with

$$\nabla\tilde{\mathcal{F}}_i = \tilde{\mathcal{A}}_{i(t)}^T * \mathcal{R}(t+1), \quad (3.2)$$

where

$$\mathcal{R}(t+1) = \begin{cases} \mathcal{R}(t) - \tilde{\mathcal{A}}_{i(t)}^T * \mathcal{X}(t) & \text{if } t \leq n \\ \mathcal{R}(t) - \tilde{\mathcal{A}}_{i(t)}^T * \mathcal{X}(t) + \tilde{\mathcal{A}}_{i(t)}^T * \mathcal{X}(t-n+1) & \text{otherwise,} \end{cases} \quad (3.3)$$

is an approximation of the residual, which only depends on one frontal slice in a fixed iteration. Then the *Frontal Slice Descent* (FSD) algorithm approximates the solution to (1.1) via the iterates

$$\mathcal{X}(t+1) = \mathcal{X}(t) + \alpha \tilde{\mathcal{A}}_{i(t)}^T * \mathcal{R}(t+1), \quad (3.4)$$

where  $\alpha \in \mathbb{R}_+$  denotes the learning rate.

The residual approximation step in our proposed method can be interpreted as a delayed computation of the exact residual, whose idea is similar to boosting in modeling literature [14, 33]. In particular, it can be shown that

$$\mathcal{R}(t+1) = \mathcal{B} - \mathcal{A} * \mathcal{X}(t-n+1) + \mathcal{E}, \quad (3.5)$$

where  $\mathcal{E}$  contains terms depending on the iterates  $\mathcal{X}(t-n+2), \dots, \mathcal{X}(t)$ , with the convention that  $\mathcal{X}(t) = 0$  for  $t \leq 0$ . Furthermore, when frontal slices are mutually orthogonal, i.e.,  $\mathcal{A}_i^T * \mathcal{A}_j = 0$ ,  $\mathcal{R}(t+1) = \mathcal{B} - \mathcal{A} * \mathcal{X}(t)$ , FSD performs similarly to gradient descent.

While the proposed method reduces data demand by removing the requirement of all  $n$  frontal slices of  $\mathcal{A}$ , its drawback is that it requires a historical memory of  $n$  versions of  $\mathcal{X}$ . In practical applications such as image and video deblurring, this drawback can be significantly circumvented due to the structure of  $\mathcal{A}$ , specifically when only a small number of frontal slices of  $\mathcal{A}$  are nonzero. See Section 5 for more details.

---

**Algorithm 3.2** Block Gradient descent with cyclic frontal slices for t-product least squares problem (1.1).

---

**Input:** data matrix  $\mathcal{A}$ , measurements  $\mathcal{B}$ , learning rate  $\alpha$ , block size  $s$   
**Initialize**  $\mathcal{R}(0) = \mathcal{B}$ ,  $\mathcal{X}(0) = \mathbf{0}$ ,  $t = 0$   
**while** stopping criteria not satisfied **do**  
     $i = \text{mod}(t, n/s) + 1$   
     $\mathcal{R}(t+1) = \mathcal{R}(t) - \tilde{\mathcal{A}}_i^s * \mathcal{X}(t) + \tilde{\mathcal{A}}_i^s * \mathcal{X}(t-n+1)$   
         $\triangleright$  Residual Approximation with the convention that  $\mathcal{X}(t) = \mathbf{0}$  for  $t \leq 0$ .  
     $\mathcal{X}(t+1) = \mathcal{X}(t) + \alpha \left( \tilde{\mathcal{A}}_i^s \right)^T * \mathcal{R}(t+1)$   $\triangleright$  Solution approximation  
     $t = t + 1$

---

### 3.2. Variations of Frontal Slice Descent

In this subsection, we present variations of the proposed approach, including using multiple frontal slices and randomly selecting slices.

**Cyclic FSD.** Our main approach iterates over the frontal slices of the tensor cyclically. By focusing on one frontal slice at a time, the proposed method simplifies the computation and reduces the immediate computational load. This cyclic approach ensures that all slices are treated uniformly over time, providing a comprehensive coverage of the tensor’s dimensions. This method might be more predictable and methodical, which can be beneficial in certain applications where systematic use of all data is crucial. The theoretical guarantees presented in Section 4 assume frontal slices are selected cyclically.

**Block FSD.** The pseudo-code for a generalized version of our proposed FSD is provided in Algorithm 3.2. Instead of using single frontal slices, our method can be extended to  $s$  frontal slices simultaneously. In particular, let

$$\tilde{\mathcal{A}}_i^s = \tilde{\mathcal{A}}_{i \cdot (s-1)+1} + \tilde{\mathcal{A}}_{i \cdot (s-1)+2} + \cdots + \tilde{\mathcal{A}}_{i \cdot s+1}, \quad (3.6)$$

denote a frontal sub-block of  $\mathcal{A}$ . When  $s = 1$ , Algorithm 3.2 simplifies to the single frontal slice setting. When  $s$  is larger, we expect that the approximation improves (See Appendix E for a discussion on blocking strategy). Algorithm 3.2 performs partial gradient updates across slices until completing a full gradient step, based on considering the decomposition of the full gradient update  $\mathcal{A}^T * (\mathcal{A} * \mathcal{X} - \mathcal{B}) = \sum_{i=1}^n \tilde{\mathcal{A}}_i^T * (\mathcal{A} * \mathcal{X} - \mathcal{B}) = \sum_{i=1}^n \tilde{\mathcal{A}}_i^T * \mathcal{R}$ . It obtains more information from  $\mathcal{A}$  per iteration compared to the single-slice Algorithm 3.2 and generalizes it. We leave the study of optimal blocking strategies for future work.

**Random FSD.** Algorithm 3.3 presents a stochastic approach where frontal slices are selected randomly in each iteration. This stochastic element can potentially lead to faster convergence in some cases. Random selection can also be more effective in dealing with tensors where certain slices are more informative than others, as it does not systematically prioritize any particular order of slices.

In this case, the memory complexity remains the same, with the requirement of storing  $n$  historical approximations  $\mathcal{X}(k_i)$  where  $k_i$  is the last iteration slice  $i$  was selected.

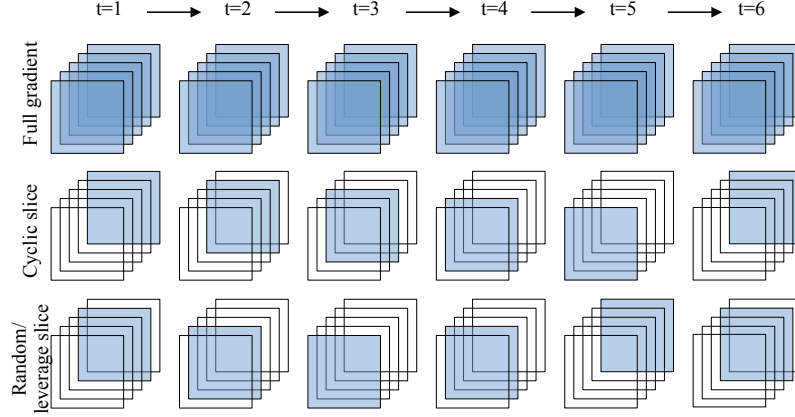


Figure 3: Algorithms 3.1, 3.2, 3.3  $t = 1, 2, 3, 4, 5, 6$  with a tensor  $\mathcal{A}$  of frontal size  $n = 5$  and block size  $s = 1$ . We illustrate the 3-way tensor with 5 frontal slices and highlight the slice at a given iteration in blue.

The residual approximate then is replaced with,

$$\mathcal{R}(t+1) = \mathcal{R}(t) - \tilde{\mathcal{A}}_i * \mathcal{X}(t) + \tilde{\mathcal{A}}_i * \mathcal{X}(k_i) \quad (3.7)$$

with the convention that  $\mathcal{X}(t) = 0$  for  $t \leq 0$ .

---

**Algorithm 3.3** Gradient descent with random frontal slices for t-product least squares problem (1.1).

---

**Input:** data matrix  $\mathcal{A}$ , measurements  $\mathcal{B}$ , learning rate  $\alpha$

**Initialize**  $\mathcal{R}(0) = \mathcal{B}$ ,  $\mathcal{X}(0) = \mathbf{0}$ ,  $k = 0 \in \mathbb{R}^n$ ,  $t = 0$

**while** stopping criteria not satisfied **do**

$i = \text{random}\{1, 2, \dots, n\}$  ▷ e.g., uniform or leverage score sampling.

$\mathcal{R}(t+1) = \mathcal{R}(t) - \tilde{\mathcal{A}}_i * \mathcal{X}(t) + \tilde{\mathcal{A}}_i * \mathcal{X}(k_i)$   
▷  $k_i$  is the last iteration slice  $i$  was selected.

▷ Residual Approximation with the convention that  $\mathcal{X}(t) = 0$  for  $t \leq 0$ .

$\mathcal{X}(t+1) = \mathcal{X}(t) + \alpha \tilde{\mathcal{A}}_i^T * \mathcal{R}(t+1)$  ▷ Solution approximation with 1  $i$ -th frontal slice

$t = t + 1$

---

### 3.3. Computational Considerations

This section summarizes storage and computational complexity for the proposed methods. To highlight the impact of the number of frontal slices  $n$ , we let  $m = \max\{n_1, n_2, n_3\}$ .

**Proposition 1.** *The computational complexity of t-product  $\mathcal{A} * \mathcal{X}$  for  $\mathcal{A} \in \mathbb{R}^{n_1 \times n_2 \times n}$  and  $\mathcal{X} \in \mathbb{R}^{n_2 \times n_3 \times n}$ . is  $\mathcal{O}(n_1 n_2 n_3 n) \sim \mathcal{O}(m^3 n)$ .*

*Proof.* We start by transforming the tensors  $\mathcal{A}$  and  $\mathcal{X}$  into the Fourier Domain. The tensors  $\mathcal{A}$  and  $\mathcal{X}$  have  $n_1n_2$  and  $n_2n_3$  tubes, respectively, each of which cost  $n \log n$  to transform to and from the Fourier Domain using FFT. Thus, these step costs  $\mathcal{O}((n_1n_2 + n_2n_3)n \log n)$  operations. Then,  $n$  matrix-matrix products are computed between frontal slices of  $\hat{\mathcal{A}}$  and  $\hat{\mathcal{X}}$ , which costs  $\mathcal{O}(nn_1n_2n_3)$ . When  $\mathcal{A}$  has  $s$  nonzero frontal slices, the complexity of the transformation to and from the Fourier Domain reduces from a dependence on  $n$  to a dependence on  $s$ . However,  $n$  matrix-matrix products are still required since frontal slices of  $\mathcal{X}$  may be dense. Thus, the computational complexity remains to be  $\mathcal{O}(nn_1n_2n_3)$ .

**Proposition 2.** *The computational complexity of each iteration in Algorithm 3.1 for  $\mathcal{A} \in \mathbb{R}^{n_1 \times n_2 \times n}$ ,  $\mathcal{X} \in \mathbb{R}^{n_2 \times n_3 \times n}$  and  $\mathcal{B} \in \mathbb{R}^{n_1 \times n_3 \times n}$  is  $\mathcal{O}(n_1n_2n_3n) \sim \mathcal{O}(m^3n)$ . The storage complexity of each iteration is  $\mathcal{O}(n_1n_2n + n_1n_3n + n_2n_3n) \sim \mathcal{O}(m^2n)$ .*

*Proof.* Using Proposition 1, the  $\mathcal{A} * \mathcal{X}(t)$  and  $\mathcal{A}^T * \mathcal{R}(t+1)$  both require  $\mathcal{O}(n_1n_2n_3n)$ . During each iteration, we need to store  $\mathcal{O}(n_1n_2n + n_1n_3n + n_2n_3n)$  arrays for  $\mathcal{A}$ ,  $\mathcal{X}(t)$ , and  $\mathcal{R}(t+1)$ .

**Proposition 3.** *The computational complexity of each iteration in Algorithm 3.2 for  $\mathcal{A} \in \mathbb{R}^{n_1 \times n_2 \times n}$ ,  $\mathcal{X} \in \mathbb{R}^{n_2 \times n_3 \times n}$  and  $\mathcal{B} \in \mathbb{R}^{n_1 \times n_3 \times n}$  is  $\mathcal{O}(n_1n_2n_3n) \sim \mathcal{O}(m^3n)$ . The storage complexity of each iteration is  $\mathcal{O}(n_1n_2s + n_2n_3n^2/s + n_1n_3n) \sim \mathcal{O}(m^2n(n/s))$ .*

*Proof.* In Algorithm 3.2, only  $s$  frontal slices of  $\mathcal{A}$  are utilized at a time, thus, the memory complexity for  $\tilde{\mathcal{A}}_i$  is  $\mathcal{O}(n_1n_2s)$  instead of  $\mathcal{O}(n_1n_2n)$ . Furthermore,  $n/s$  historical approximations of  $\mathcal{X}$  need to be stored. Thus, the total memory complexity is  $\mathcal{O}(n_1n_2s + n_2n_3n^2/s + n_1n_3n)$ .

**Corollary 4.** *The computational complexity of each iteration in Algorithm 3.2 ( $s = 1$ ) and 3.3 for  $\mathcal{A} \in \mathbb{R}^{n_1 \times n_2 \times n}$ ,  $\mathcal{X} \in \mathbb{R}^{n_2 \times n_3 \times n}$  and  $\mathcal{B} \in \mathbb{R}^{n_1 \times n_3 \times n}$  is  $\mathcal{O}(n_1n_2n_3n) \sim \mathcal{O}(m^3n)$ , The storage complexity of each iteration is  $\mathcal{O}(n_1n_2 + n_2n_3n^2 + n_1n_3n) \sim \mathcal{O}(m^2n^2)$ .*

Since  $\tilde{\mathcal{A}}_i^s$  may be dense, the use of frontal slices does not necessarily reduce computational complexity, but reduce the communication cost.

**Corollary 5.** *Suppose  $\mathcal{A}$  has  $k \ll n$  nonzero frontal slices then, the computational complexity of each iteration in Algorithm 3.2 (with  $s = 1$ ) and 3.3 is  $\mathcal{O}(n_1n_2n_3n) \sim \mathcal{O}(m^3n)$ , for  $\mathcal{A} \in \mathbb{R}^{n_1 \times n_2 \times n}$ ,  $\mathcal{X} \in \mathbb{R}^{n_2 \times n_3 \times n}$  and  $\mathcal{B} \in \mathbb{R}^{n_1 \times n_3 \times n}$ . The storage complexity of each iteration is  $\mathcal{O}(n_1n_2 + n_2n_3k^2 + n_1n_3n) \sim \mathcal{O}(m^2k^2)$ .*

## 4. Convergence Analysis

Theorem 6 provides the main convergence guarantees for the cyclic FSD algorithm (Algorithm 3.2) when  $s = 1$ . Theorem 8 presents the special case in which  $n = 2$ , and Corollary 7 extends our results to the block FSD case ( $s > 1$ ). For an appropriately chosen learning rate  $\alpha > 0$ , show that  $\mathcal{X}(k)$  converges to the solution  $\mathcal{X}_*$  and obtain a

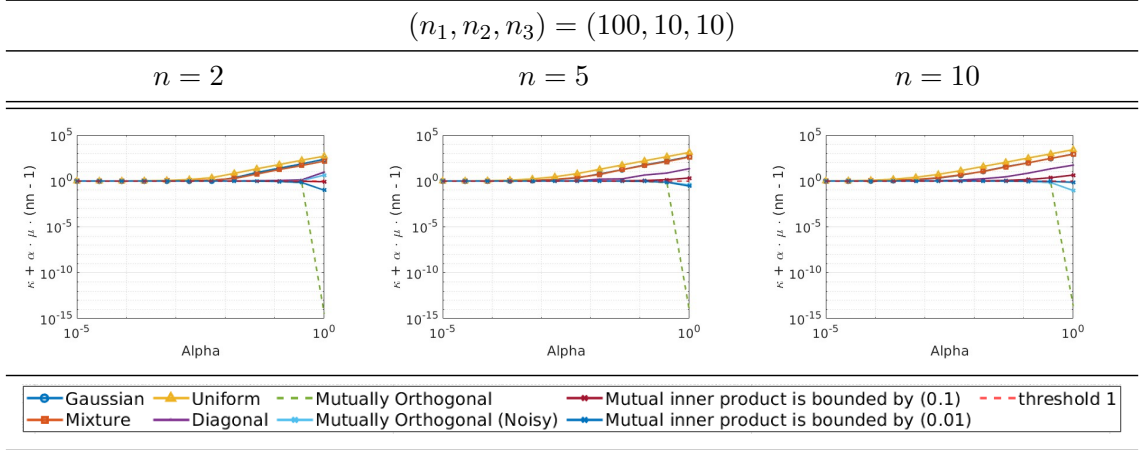


Figure 4: The bound of learning rate  $\alpha$  as shown in Theorem 6 for Algorithm 3.2 to tensor  $\mathcal{A}$  with (1) i.i.d Gaussian entries (2) i.i.d. Unif[0,1] entries, and (3) an additive mixture between Gaussian and uniform entries. We also provide synthetic cases where  $\mathcal{A}$  has (4) frontal slices, which are each diagonal matrices (5) mutually orthogonal frontal slices (w.r.t. matrix inner product) (6) mutual inner products between frontal slices are bounded by 0.1 (7) mutual inner products between frontal slices are bounded by 0.01 (8) mutually orthogonal frontal slices with Gaussian noise.

convergence result in the following theorem. This is accomplished by showing approximation error  $\mathcal{E}(t) = \|\mathcal{X}(t) - \mathcal{X}^*\|_F^2$  converges to 0, where  $\mathcal{X}^*$  is the actual solution to the consistent system (1.1). Since we are handling a finite dimensional system, it is obvious that  $0 < \mathcal{E}(0) < \infty$  by definition.

**Theorem 6** (Convergence of cyclic-FSD). *Let  $\mathcal{A} * \mathcal{X} = \mathcal{B}$  be a consistent tensor system with unique solution  $\mathcal{X}^*$  where  $\mathcal{A} \in \mathbb{R}^{n_1 \times n_2 \times n}$  and  $\mathcal{B} \in \mathbb{R}^{n_1 \times n_3 \times n}$ . Define  $\epsilon_t$  to be the coefficient such that  $\mathcal{E}(t+1) \leq \epsilon_t \mathcal{E}(0)$  and let*

$$\kappa = \max_{i=1, \dots, n} \|\mathcal{I} - \alpha \tilde{\mathcal{A}}_i^T * \tilde{\mathcal{A}}_i\|_{op}, \quad (4.1)$$

$$\mu = \max_{\substack{i, j=1, \dots, n \\ i \neq j}} \|\tilde{\mathcal{A}}_i^T * \tilde{\mathcal{A}}_j\|_{op}. \quad (4.2)$$

*If the learning rate  $\alpha$  is chosen such that  $\kappa + \alpha\mu(n-1) < 1$ , then  $\mathcal{E}(t) \rightarrow 0$  as  $t \rightarrow \infty$ .*

*Proof.* See Appendix C.

Since  $\kappa$  is also a function of learning rate  $\alpha$ , we want to ensure that assumption  $\kappa + \alpha\mu(n-1) < 1$  in Theorem 6 is feasible. When  $\mu = 0$ , the frontal slices of the coefficient tensor  $\mathcal{A}$  are mutually orthogonal frontal slices (w.r.t. matrix inner product). In this case, the sufficient condition in Theorem 6 becomes trivial when  $\alpha$  is selected so that  $\kappa < 1$ . This gives us a wide range of choices of  $\alpha$  as shown by Figure 4 case (5). Another extreme occurs when the frontal slices are each diagonal matrices in case (4),

making  $\kappa$  exceed 1 easily, and we can see that such a situation will always violate the sufficient bound.

Beyond cases (4) and (5), cases (6) and (7) allow for approximate orthogonality. Here, the frontal slices are almost orthogonal, up to a matrix inner product threshold. As the frontal size  $n$  increases, we need to set this inner product threshold to be smaller such that  $\mu(n-1)$  falls in a reasonable range. Another scenario case (8) is created by perturbing the case (4) using a standard Gaussian noise tensor (like case (1)) multiplied by  $\frac{1}{n^3}$ , also creating a scenario where our sufficient bound for  $\alpha$  can be met.

Unfortunately, the more usual cases like (1) to (3) in Figure 4 will not satisfy our sufficient condition in Theorem 6; yet we will see in the next section (i.e., Figure 7) that even if our sufficient condition on the learning rate  $\alpha$  does not hold, Algorithm 3.2 and its variants still yields reasonable convergence rates with fixed  $\alpha$ . This makes it a well-defined future work to find the necessary condition for the learning rate  $\alpha$ .

Corollary 7 presents the convergence of the blocked case  $2 \leq s < n$  in Algorithm 3.2.

**Corollary 7.** For  $n \geq 2$  and  $2 \leq s < n$  in Algorithm 3.2, we define  $\tilde{\mathcal{A}}_i^s := \tilde{\mathcal{A}}_{i.(s-1)+1} + \tilde{\mathcal{A}}_{i.(s-1)+2} + \dots + \tilde{\mathcal{A}}_{i.s}$  to be the sum of  $s$  padded slices and

$$\kappa(s) = \max_{i=1, \dots, n/s} \|\mathcal{I} - \alpha \tilde{\mathcal{A}}_i^{sT} * \tilde{\mathcal{A}}_i^s\|_{op}, \quad (4.3)$$

$$\mu(s) = \max_{\substack{i,j=1, \dots, n/s \\ i \neq j}} \|\tilde{\mathcal{A}}_i^{sT} * \tilde{\mathcal{A}}_j^s\|_{op}. \quad (4.4)$$

Suppose that the learning rate  $\alpha$  is chosen such that

$$\kappa(s) + \alpha \mu(s)(n/s - 1) < 1.$$

Then, we have  $\lim_{t \rightarrow \infty} \mathcal{E}(t) = 0$ .

*Proof.* See Appendix E.

When  $n = 2$ , by Theorem 6, we have that Algorithm 3.2 converges to the solution to the consistent system (1.1) as  $t \rightarrow \infty$  as long as  $\alpha$  is chosen such that  $\kappa < 1$  and  $\alpha < \frac{1-\kappa}{\mu}$ . In the  $n = 2$  case, we can also place additional constraints on the learning rate  $\alpha$  to determine the convergence rate per  $n$  iterations.

**Theorem 8.** Define  $\kappa_1 = \|\mathcal{I} - \alpha \tilde{\mathcal{A}}_1^T * \tilde{\mathcal{A}}_1\|_{op}$ ,  $\kappa_2 = \|\mathcal{I} - \alpha \tilde{\mathcal{A}}_2^T * \tilde{\mathcal{A}}_2\|_{op}$  and  $\mu = \|\tilde{\mathcal{A}}_1^T * \tilde{\mathcal{A}}_2\|_{op}$ . If  $\alpha < \min\{\frac{1-\kappa_2}{\mu}, \frac{1-\kappa_1\kappa_2}{\mu(1+\kappa_2)}\}$  then we have  $\lim_{t \rightarrow \infty} \mathcal{E}(t) = 0$ . Furthermore, assume that  $\mathcal{M}(0) < \infty$  for

$$\mathcal{M}(t) = \max\{\mathcal{E}(2t), \mathcal{E}(2t+1)\},$$

$\mathcal{M}(t)$  converges at a rate of  $C = \max\{\kappa_2 + \alpha\mu, \kappa_1\kappa_2 + (1 + \kappa_1)\alpha\mu\} < 1$ .

*Proof.* See Appendix B.

The proof of Theorem 8 is provided in Appendix B. Note that the  $\kappa_1, \kappa_2$  contains the learning rate  $\alpha$  and therefore the sufficient condition  $\alpha < \min\{\frac{1-\kappa_2}{\mu}, \frac{1-\kappa_1\kappa_2}{\mu(1+\kappa_2)}\}$  requires

solving this inequality. It implies that the range of  $\alpha$  where an algorithm converges is determined by the  $\|\tilde{\mathcal{A}}_i^T * \tilde{\mathcal{A}}_i\|$  ( $i = 1, 2$ ) and  $\mu = \|\tilde{\mathcal{A}}_1^T * \tilde{\mathcal{A}}_2\|_{op}$ , which are the norms of each (padded) frontal slice and correlations between the (padded) frontal slices of the coefficient tensor in the system (1.1).

In Theorem 8, in addition to the limiting error converging to zero, we can also observe that the norms  $\|\tilde{\mathcal{A}}_i^T * \tilde{\mathcal{A}}_i\|$  ( $i = 1, 2$ ) and correlation  $\mu$  between frontal slices jointly determine the convergence rate of the Algorithm 3.2. When the norm is larger, the  $\kappa$  tends to be smaller, and the convergence rate becomes smaller; when the correlation  $\mu$  is smaller, the convergence rate becomes smaller. The same idea also applies when we compare the convergence rates of  $s = 1, s > 1$  cases. The convergence rates are dominated by  $\kappa(s)^t < \kappa^t$ , indicating that single-slice descent indeed sacrifices the convergence rate to only work with one frontal slice of  $\mathcal{A}$  at a time.

When the system is inconsistent, there will be an additional error term in the bound, which creates a convergence horizon. In this more realistic scenario where the system is corrupted by noise, the choice of  $\mathcal{X}(0)$  and hence  $\mathcal{E}(0)$  will affect the convergence behavior.

**Theorem 9.** *Let  $\kappa, \mu$  be defined as in Theorem 6 and suppose that Algorithm 3.2 with  $s = 1$  is applied to the inconsistent linear system  $\mathcal{A} * \mathcal{X} = \mathcal{B} + \mathcal{B}_e$ , with solution  $\mathcal{X}^*$  such that  $\mathcal{A} * \mathcal{X}^* = \mathcal{B}$ . Define  $\eta_t \in \mathbb{R}$  such that  $\mathcal{E}(t+1) \leq \eta_t \mathcal{E}(t) + \alpha \eta_e$  where  $\eta_e = \max_{i=1, \dots, n} \|\tilde{\mathcal{A}}_i\|_{op} \|\mathcal{B}_e\|$ . If the learning rate  $\alpha$  is selected such that  $\kappa + \alpha \mu(n-1) + \frac{\alpha}{\mathcal{E}(0)} \eta_e < 1$  then as  $t \rightarrow \infty$ ,  $\mathcal{E}(t) \rightarrow \alpha \eta_e$ .*

*Proof.* See Appendix D.

When frontal slices are selected at random, without replacement, the same proof argument follows by relabeling the frontal slices after each  $n$  iterations. However, the proof of the randomized case with replacement is nontrivial without additional or restrictive assumptions. We leave the proofs of this case as future work.

## 5. Experiments

In this section, we perform a collection of numerical experiments on synthetic and real-world data sets to demonstrate and compare the application of the proposed methods. In our experiments, unless otherwise noted, we fix  $n_1, n_2, n_3$ , and  $n$ . The first set of experiments pertain only to the performance of FSD. The first is a study of the algorithm with varying step sizes, the second investigates the algorithm's performance when key parameters in our theoretical guarantees ( $\kappa$  and  $\mu$ ) vary, and the last investigates the performance deterioration as  $n$  grows. The second two experiments compare the variations of FSD and then FSD with other sketching approaches. The last two experiments evaluate the performance of FSD on image and video deblurring, where only a small number of frontal slices of  $\mathcal{A}$  are non-zero due to the nature of the deblurring operator, thus making it a prime case where FSD can be efficiently applicable.



## 5.1. Synthetic Experiments

For all synthetic experiments, unless otherwise noted, the entries of  $\mathcal{A}$  and  $\mathcal{X}$  are drawn i.i.d. from a standard Gaussian distribution,  $\mathcal{X}$  is normalized to have unit Frobenius norm, and we set  $\mathcal{B} = \mathcal{A} * \mathcal{X}$  to generate consistent systems.

Our first synthetic experiment demonstrates the performance of Algorithm 3.2 on a Gaussian system with varying learning rates and dimensions. The three different dimension configurations provide insight into how the tensor’s structure affects the methods’ performance. In general, we observe that when the frontal size ( $n$ ) is moderate ( $n = 10$ ), the performance varies slightly among methods but follows a general trend of decreasing error with more iterations. When the frontal size ( $n$ ) is increased ( $n = 20$ ), the performance differences become more pronounced. When the column size ( $n_2$ ) is larger ( $n_2 = 20$ ), leverage score sampling tends to perform better, suggesting that this method handles higher column dimensions effectively.

For  $\alpha=0.5$  (except for TRK), all FSD methods show a gradual decrease in error, but the convergence is slower compared to higher learning rates. For  $\alpha = 1$ , the convergence speeds up, and the TRK method still consistently outperforms others, achieving the lowest approximation error. For  $\alpha = 2$ , the convergence becomes fast, but there are instances of oscillation, which suggests instability at higher learning rates. The cyclic FSD demonstrates the best performance, maintaining stability and achieving low errors. When we keep increasing the learning rate of FSD methods to  $\alpha = 4$ , then cyclic FSD along with its variants outperforms TRK in most cases.

Overall, the results indicate that the cyclic and leverage score sampling methods perform well, particularly when the column size is large. The TRK method shows competitive performance at lower learning rates but becomes unstable at higher learning rate  $\alpha$ . Random sampling and cyclic methods perform adequately but generally lag behind leverage score sampling in terms of convergence speed and final error. These findings suggest that choosing the appropriate method and tuning the learning rate based on the tensor’s dimensions can significantly improve performance in solving large-scale tensor systems.

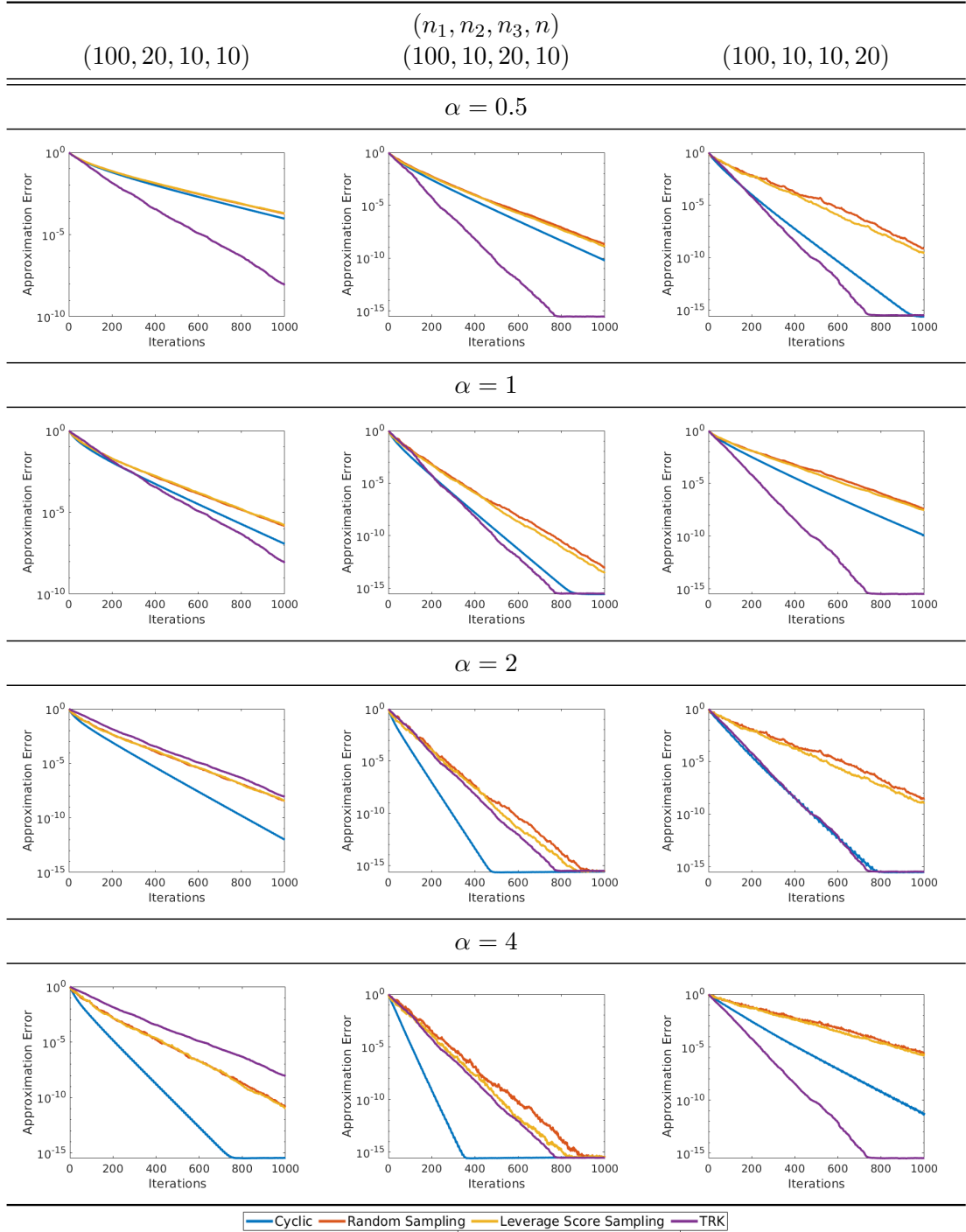


Figure 5: Generate  $\mathcal{A}, \mathcal{X}$  and compute consistent  $\mathcal{B} = \mathcal{A} * \mathcal{X}$  for the synthetic system for varying dimension sizes. In each panel, we show the final approximation error  $\mathcal{E}(T)$  using different methods (Frontal: Algorithm 3.2; Sample (Random): Algorithm 3.3 with uniform random sampling of slices; Sample (Leverage): Algorithm 3.3 with leverage score sampling of slices; TRK: [36]) and learning rate  $\alpha = 0.001$  and the maximal number of iterations of 1000 steps. Comparison of performance of different iterative methods for solving tensor systems when  $n_1 = 100, n_2 = 20, n_3 = 10, n = 10$ , and  $\alpha = \{0.5, 1, 2, 4\}$  for frontal descent methods

Figure 6 shows the performance of Algorithm 3.2 when varying the number of frontal slices. In this experiment, we plot the final approximation error after 1000 iterations and averaged over 20 runs for each values of  $n$  and present the average approximation error  $\|\mathcal{X}(1000) - \mathcal{X}_*\|_F$ . We expect that as the number of frontal slices increases, the per-iteration approximation quality of the residual deteriorates. Thus, it is expected that the final approximation error after 1000 iterations and  $\alpha = 0.001$  increases as  $n$  increases, as shown in Figure 6.

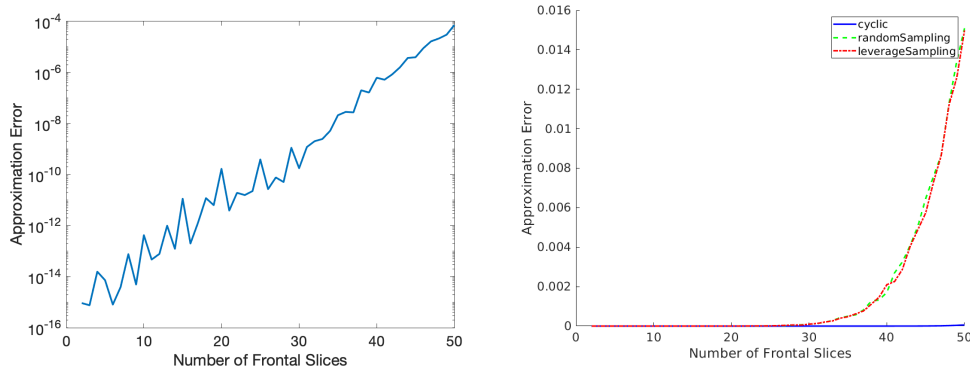


Figure 6: Performance of Algorithm 3.2 (left), 3.3 (right: joint comparison between cyclic, uniform and leverage score sampling) on an i.i.d. Gaussian system with  $n_1 = 100$ ,  $n_2 = 20$ ,  $n_3 = 10$ ,  $\alpha = 0.001$ , and varying  $n$  averaged over 20 different seeds. As the frontal size increases, the approximation errors at the end of (the same maximal number of) iterations also increase.

Our next experiment considers different types of measurement tensors  $\mathcal{A}$ , which exhibit different  $\kappa$  and  $\mu$ . In this experiment, we fix  $n_1 = 100$ ,  $n_2 = 20$ ,  $n_3 = 10$ ,  $n = 10$ , and  $\alpha = 0.0001$  while applying Algorithm 3.2 to tensors with (1) i.i.d Gaussian entries (2) i.i.d. Unif[0,1] entries and (3) an additive mixture between Gaussian and uniform entries. The accompanying table in Figure 7 shows the values of  $\kappa$  and  $\mu$  for the randomly generated systems while Figure 7 presents the performance of Algorithm 3.2 for the different types of systems. Note that for Gaussian systems, where  $\mu$  is small, the proposed method works quite well, whereas it converges slower for systems in which  $\mu$  is larger, such as the Uniform system. In particular, we can compute the numerical approximation (via an optimizer for obtaining the maximum over the sphere  $\|\mathcal{X}\|_{op}$ ) of the quantities (4.1) and (4.2). The scatter plot in Figure 7 visualizes systems with different  $\kappa$  and  $\mu$  values, generated using Gaussian, Mixture, and Uniform distributions. The x-axis represents  $\kappa$  and the y-axis represents  $\mu$ , with dot colors indicating the final approximation error. Gaussian systems, represented by circles, cluster towards lower  $\kappa$  and  $\mu$  values, displaying relatively low approximation errors (darker blue colors). Mixture systems, represented by squares, have slightly higher  $\kappa$  and  $\mu$  values than Gaussian systems but still maintain low errors. Uniform systems, shown as triangles, spread out with significantly higher  $\kappa$  and  $\mu$  values, exhibiting a wider range of approximation errors, with some reaching higher values (yellow shades). This plot effectively demonstrates

that Gaussian and Mixture systems yield lower  $\kappa$  and  $\mu$  values and lower approximation errors, while Uniform systems display higher values and more variability in their errors, highlighting the impact of system type on tensor approximation performance. Note that the learning rate  $\alpha$  does not fall in the sufficient convergence horizon in Theorem 6, yet we still observe convergence, which indicates that a sharper horizon is possible.

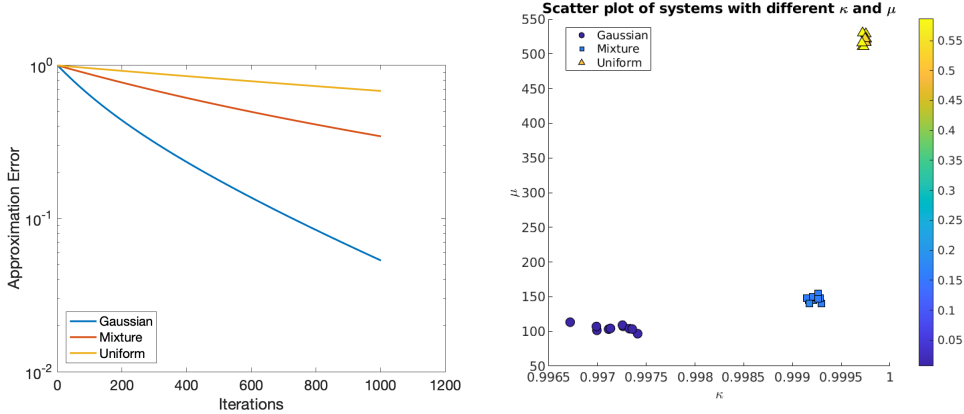


Figure 7: Performance of Algorithm 3.2 (block size=1) with different types of tensors  $\mathcal{A}$  when  $n_1 = 100$ ,  $n_2 = 20$ ,  $n_3 = 10$ ,  $n = 10$ , and  $\alpha = 5 \times 10^{-5}$ . Left: We provide the numerical approximation to the operator norms  $\kappa$  and  $\mu$  for each system as defined in 4.1 and 4.2. Right: The scatter plot visualizes the systems with different  $\kappa$  and  $\mu$  values, generated using Gaussian, Mixture, and Uniform distributions. Each dot’s color indicates the final approximation error, with the color bar on the right showing the error scale.

Figure 8 presents the performance of Algorithm 3.2 with varying block sizes  $s$ . The measurement tensor  $\mathcal{A}$  is i.i.d. Gaussian with  $n = 10$  frontal slices. Thus, when  $s = 10$ , Algorithm 3.2 with blocking is equivalent to Algorithm 3.1. Intuitively, we have more information when we have larger block sizes, larger block sizes allow the algorithm to converge faster since the residual approximations improve as  $s$  increases. In terms of convergence horizon, we need fewer assumptions to check for  $\kappa, \mu$  and hence enjoy a wider horizon of convergence (See details in Appendix E).

Our last synthetic experiment compares the variations of the proposed method with the TRK algorithm [36]. Since the TRK algorithm assumes row slices are normalized, we incorporate the row normalization for each row slice and increase the learning rate  $\alpha = 3$  for all variations of frontal slice descent. Figure 5 presents the performance of Algorithm 3.2 (“Cyclic”), Algorithm 3.3 with leverage score sampling, Algorithm 3.3 with simple random sampling, and TRK on a Gaussian system when  $n_1 = 100$ ,  $n_2 = 20$ ,  $n_3 = 10$ , and  $n = 10$ . In this case, we observe that Algorithm 3.2 and Algorithm 3.3 perform similarly as shown in Figure 5, and most importantly, that all three methods are converging to the solution. It should be noted that the choice of learning rate impacts which method outperforms the other (choosing a smaller learning rate may lead to Algorithm 3.2 to converge slower than TRK, see, for example, Figure 9).

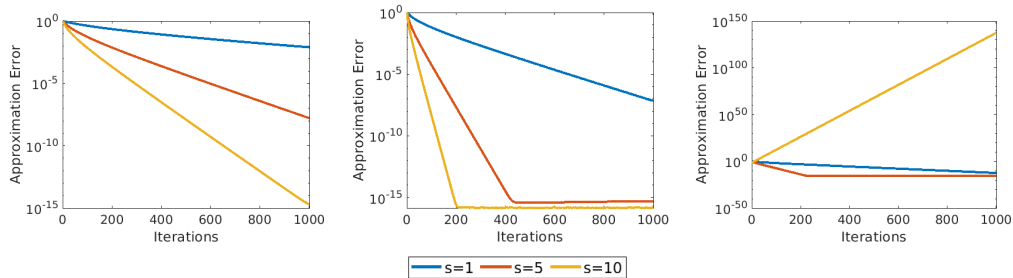


Figure 8: Performance of Algorithm 3.2 with different frontal block sizes  $s$  when  $n_1 = 100$ ,  $n_2 = 20$ ,  $n_3 = 10$ ,  $n = 10$ , and  $\alpha = 0.0001, 0.0005, 0.001$ .

$n$	1	10	100	1000
Frontal: Algorithm 3.2	0.016734	0.030362	0.089839	0.743340
Sample (Random): Algorithm 3.3	0.015908	0.031074	0.096795	0.739575
Sample (Leverage): Algorithm 3.3	0.015652	0.030578	0.092100	0.730805
TRK: [36]	0.003110	0.003010	0.015947	0.013112

Table 1: The system wall-clock time (seconds via tic-toc) of each algorithms for 1000 iterations on a system with  $n_1 = n_2 = n_3 = 100$ , but with increasing  $n$ . This time is averaged over 5 repeated experiments.

**Remark 2.** The TRK algorithm uses exact residual information for its updates, which can lead to more precise and potentially faster convergence as shown in Table 1. In contrast, the method discussed in this paper does not utilize exact residual information, which may lead to slower convergence or less accurate updates. The frontal sketching methods discussed in Algorithms 3.2 and 3.3 may perform worse than TRK because they doesn't use exact residual information (See Figure 5).

**Remark 3.** The varying  $n_3$  should not affect the convergence result that much, since our main theorems (in Section 3) bounds the convergence rate using information of the tensor  $\mathcal{A}$  only, which only involves  $n_1, n_2, n$ . The performance of matrix sketching methods depends on the aspect ratio, specifically the number of rows ( $n_1$ ) to columns ( $n_2$ ). For tensor sketching, similar principles apply, involving the row/frontal ( $n_1/n$ ) and column/frontal ( $n_2/n$ ) ratios. These ratios affect both computational efficiency and convergence rates. In tensor algorithms like frontal slice descent, higher row/frontal or column/frontal ratios can lead to better-conditioned sub-problems and faster convergence, but at a higher computational cost per iteration. Optimizing these aspect ratios is crucial for improving the performance of tensor-based sketching methods in practical applications. For example, if  $n_1 = 100$  (rows) and  $n_2 = 20$  (columns), and given the effective frontal size of  $n = 10$ , the effective row/frontal ratio is  $100/10 = 10$ , and the effective column/frontal ratio is  $20/10 = 2$ . Since the effective column/frontal ratio is

*smaller, column sketching might be more appropriate despite the large nominal frontal size. This approach considers both actual and effective sizes, optimizing the sketching method based on correlation.*

## 5.2. Real World Application: Deblurring

In many imaging problems, particularly those involving inverse operations such as image deblurring or reconstruction, the problem is often ill-posed. This typically happens because the forward model (the process that generates the observed data from the true image) is not invertible or is sensitive to noise. For example, if multiple images can produce similar observed data, then the problem lacks a unique solution. As another example, if small changes or noise in the observed data lead to large changes in the reconstructed image, then the problem lacks stability. An example of such an imaging problem is *deblurring*, where the objective is to recover the original version of an image that has been blurred. Traditional methods often struggle with recovering high-quality images from blurred observations, especially when dealing with tensor data structures.

The t-product’s convolutional nature is particularly useful in imaging problems because it aligns with the structure of typical imaging operations. Convolution operations in imaging can be represented as circulant matrices, which naturally align with the t-product formulation. This alignment is particularly beneficial for ill-posed imaging problems, where the convolution represents the blurring or transformation applied to an image. A blurring operator, designed using Gaussian kernels (of fixed band-width and noise variance on the normalized scale), is applied to each slice of the resized tensor to simulate a blurred video. The algorithms aim to solve the tensor equation  $\mathcal{A} * \mathcal{X} = \mathcal{B}$ , where  $\mathcal{B}$  is the observed blurred tensor,  $\mathcal{A}$  is the blurring operator (which can be represented as a tensor operation via t-product), and  $\mathcal{X}$  is the original noiseless tensor in (1) or (2). Error metrics are calculated for each slice by comparing the recovered slices with the original slices and then averaged over all slices. The error metrics for each algorithm are averaged over all slices to provide a comprehensive assessment. Lower MSE values and higher PSNR and SSIM values indicate better recovery quality. The metrics are defined as follows:

- **MSE** measures the average squared difference between the original and recovered pixel values. Lower values indicate closer resemblance to the original image.
- **PSNR** is a logarithmic measure of the ratio between the maximum possible pixel value and the power of the noise (error). Higher values indicate less noise in the recovered image.
- **SSIM** evaluates the structural similarity between the original and recovered images, taking into account luminance, contrast, and structure. Values range from -1 to 1, with higher values indicating better structural similarity.

Given the t-product structure, [41] develops several algorithms for solving such ill-posed t-product linear systems, including Tikhonov Regularization with Arnoldi (tAT), Generalized Minimal Residual (tGMRES) Methods and their global variants. However, these

are regularized methods; we will show how the performance of exact sketching solvers behave in this experiment. In this section, we compare the use of frontal slices and row slices to image deblurring applications. The generation of the blurring operator  $\mathcal{A}$  closely follows that outlined in [41], and we present the details here for completion. Given parameters  $\sigma, N$ , and  $B$ , the tensor  $\mathcal{A} \in \mathbb{R}^{N \times N \times N}$  is generated with frontal slices

$$\mathcal{A}_i = A_1(i, 1)A_2 \quad i = 1, \dots, N,$$

where matrices  $A_1$  and  $A_2$  are generated by the Matlab commands:

$$\begin{aligned} \mathbf{z}_1 &= [\exp(-([0 : \text{band} - 1].^2)/(2\sigma^2)), \text{zeros}(1, N - B)], \\ \mathbf{z}_2 &= [\mathbf{z}_1(1) \text{fliplr}(\mathbf{z}_1(\text{end} - \text{length}(\mathbf{z}_1) + 2 : \text{end}))], \\ A_1 &= \frac{1}{\sigma\sqrt{2\pi}} \text{toeplitz}(\mathbf{z}_1, \mathbf{z}_2), \\ A_2 &= \frac{1}{\sigma\sqrt{2\pi}} \text{toeplitz}(\mathbf{z}_1) \end{aligned}$$

and  $B$  and  $\sigma$  determine the band size and variation in the Gaussian blur, respectively. It should be noted that the frontal slices are extremely ill-conditioned: the first  $B + 1$  frontal slices have conditioning  $\approx 10^6$ , and the remaining frontal slices are all zeros. Since the proposed methods are frontal slice-based, we only need to cycle through the first  $B + 1$  frontal slices of  $\mathcal{A}$ .

Our experiments demonstrate that tensor recovery algorithms can effectively deblur and recover images from blurred observations. The metrics used provide a quantitative assessment of the recovery quality, with lower MSE and higher PSNR and SSIM values indicate better performance. These findings are valuable for applications in image processing and computer vision, where high-quality image recovery is essential.

Figure 9 compares the performance of Algorithm 3.2 and TRK on image deblurring. The image is a resized version of the  $512 \times 512$  pixel image of the Hubble Space Telescope in Figure 2. The measurements  $\mathcal{B} = \mathcal{A} * \mathcal{X}$  where  $\mathcal{A}$  is the  $151 \times 151 \times 151$  blurring operator with  $B = 9$  and  $\sigma = 3$ . The learning rate is selected to be  $\alpha = 0.01$ . We put the initial image with double precision where the image is extended into a 3-way tensor by creating several slices (frames) with slight variations introduced by Gaussian additive noise.

## 100 by 100 resized HST Satellite Image from [41]

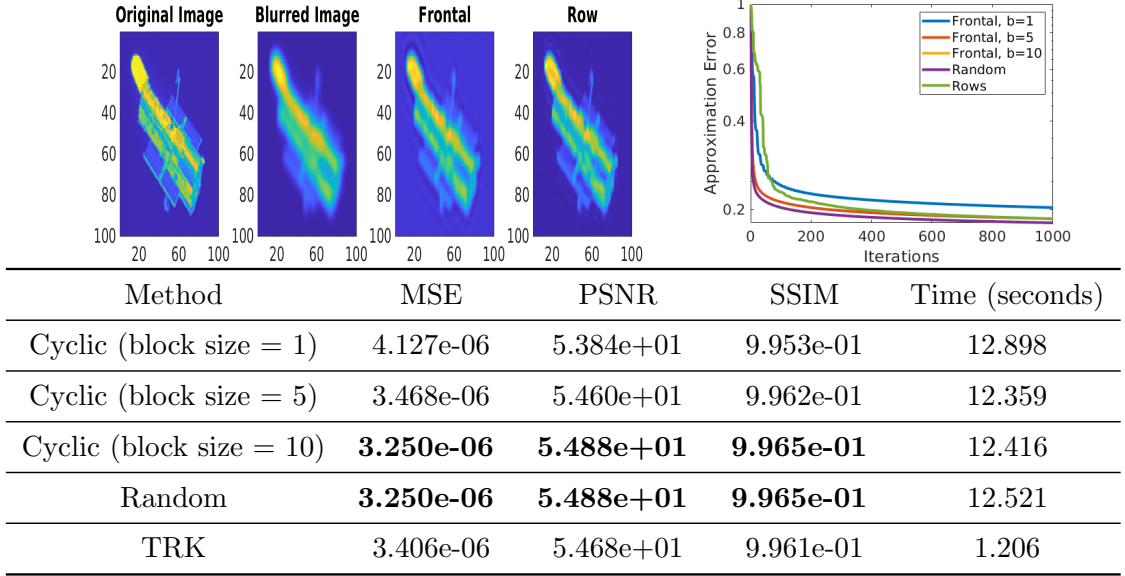


Figure 9: HST Satellite Image from [41]. A frontal slice (i.e., frame) from the resized ground truth video  $\mathcal{X}[:, :, 15] \in \mathbb{R}^{60 \times 60 \times 1}$ , the blurred video  $\mathcal{B}[:, :, 15] \in \mathbb{R}^{60 \times 60 \times 1}$ , the recovered slice when using cyclic frontal slice descent (Algorithm 3.2), random frontal slice descent (Algorithm 3.3), and when using TRK [36]. In the leftmost panel, we show the final approximation error  $\mathcal{E}(T)$  against iterations with learning rate  $\alpha = 0.01$  and the maximal number of iterations of 1000 steps.

## 151 by 31 by 151 full-size trimmed video

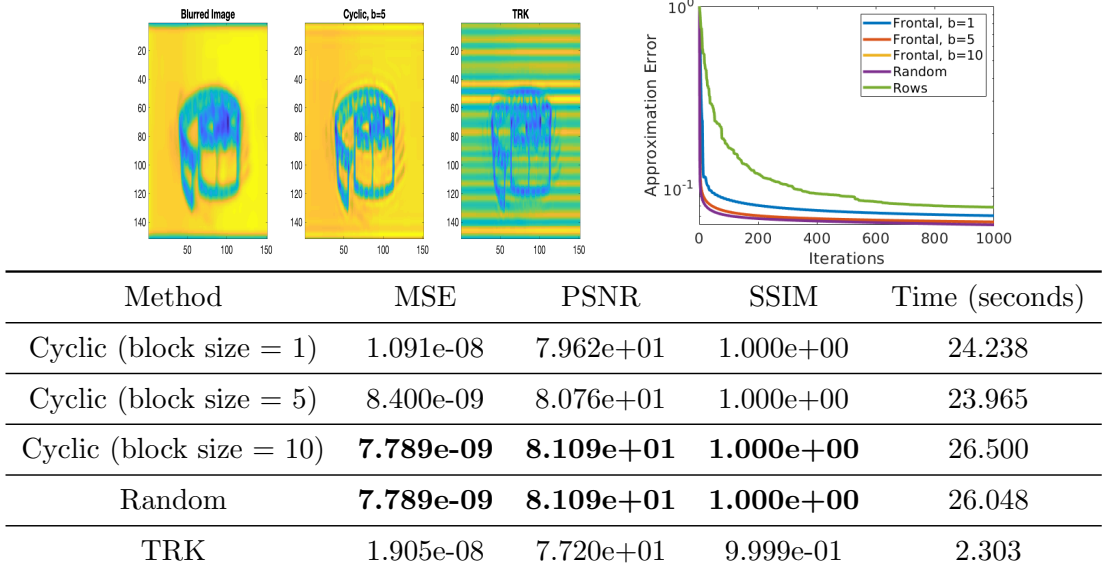


Figure 10: Trimmed video tensor. Top: A frontal slice (i.e., frame) from the resized ground truth video  $\mathcal{X}[:, :, 15] \in \mathbb{R}^{60 \times 60 \times 1}$ , the blurred video  $\mathcal{B}[:, :, 15] \in \mathbb{R}^{60 \times 60 \times 1}$ , the recovered slice when using cyclic frontal slice descent (Algorithm 3.2), random frontal slice descent (Algorithm 3.3), and when using TRK [44]. In the leftmost panel, we show the final approximation error  $\mathcal{E}(T)$  against iterations with learning rate  $\alpha = 0.01$  and the maximal number of iterations of 1000 steps. Bottom: A frontal slice (i.e., frame) from the ground truth video  $\mathcal{X}[:, :, 15] \in \mathbb{R}^{151 \times 151 \times 1}$ , the blurred video  $\mathcal{B}[:, :, 15] \in \mathbb{R}^{151 \times 151 \times 1}$ , the recovered slice when using CFGD and TRK. In the leftmost panel, we show the final approximation error  $\mathcal{E}(T)$  against iterations with learning rate  $\alpha = 0.001$  and the maximal number of iterations of 200 steps.



In Figure 10, we apply TRK and Algorithm 3.2 on video data containing frames from the 1929 film “Finding His Voice” [9]. The video is the underlying tensor  $\mathcal{X}$  with 31 video frames, each of size  $151 \times 151$ . The measurements  $\mathcal{B} = \mathcal{A} * \mathcal{X}$  where  $\mathcal{A}$  is the  $151 \times 151 \times 151$  blurring operator with  $B = 9$  and  $\sigma = 4$ . The learning rate is selected to be  $\alpha = 0.001$ . While both suffer from the ill-conditioned nature of  $\mathcal{A}$ , Algorithm 3.2 can attain a smaller error faster than TRK.

In addition, the visual quality of the recovery of the proposed method is better than that of TRK, which can be seen in the convergence plot in Figure 10. Figure 10 presents the original 15th video frame  $\mathcal{X}[:, :, 15]$ , the blurred video frame,  $\mathcal{B}[:, :, 15]$ , the recovered slice when using Algorithm 3.2, and when using TRK. The goal is to recover the original image, represented as a tensor  $\mathcal{X}$ . The blurred image is  $\mathcal{B}$ , and the blurring operation is represented by the tensor  $\mathcal{A}$ . The t-product formulation naturally models this convolutional process, allowing for efficient algorithms to deblur the image by solving (1.1) given known  $\mathcal{A}$  and  $\mathcal{B}$ . The convolutional nature of the t-product effectively captures the blurring effect and facilitates the subsequent reconstruction of the original image through iterative methods that utilize the convolutional structure.

## 6. Conclusion and Future works

Our exploration of tensor sketching methods has highlighted the potential of frontal sketching, but comparable analyses with row and column sketching methods remain less developed. A crucial area for future research involves establishing a robust criterion that would allow for the selection between frontal, row, and column sketching methods based on specific data characteristics or performance metrics.

The primary goal will be to develop and validate a set of criteria or metrics that can effectively determine the optimal sketching technique for a given tensor dataset and application. These criteria may include, but are not limited to, considerations of computational efficiency, memory usage, data sparsity, and the preservation of tensor properties critical to the application domain. Besides finding a necessary condition for the learning rate in our sketching algorithms, another goal is integrating adaptive learning rates  $\alpha$  (which varies as iterations proceeds) into the dynamic sketching algorithm, where not only the sketching method is chosen adaptively, but also the learning rates are adjusted based on real-time feedback from the sketching process, which has an intrinsic link to sparse likelihood approximation when certain kind of sparsity is encoded in the system [7, 33, 34].

Building on the established criteria, the next phase will involve designing an adaptive sketching algorithm. This algorithm will dynamically switch between frontal, row, and column sketching based on real-time analysis of the data’s evolving characteristics during processing. Such adaptability could significantly enhance performance in diverse scenarios, ranging from real-time data streaming to large-scale data processing where different sketching methods may be optimal at different processing stages.

Although higher-order t-products can be defined in a recursive manner, extending the sketching methods in the current work for higher-order tensor t-products generate

new challenges. The complexity of defining and computing such products increases significantly with the tensor order, thus computational complexity and numerical stability becomes a critical issue and careful consideration of algorithmic design and tensor operations are needed. In addition, the t-product leverages the block circulant matrix representation of tensors, where each frontal slice of a tensor is shifted and concatenated to form a larger block circulant matrix, which can be seen as a form of circular convolution applied along the third dimension (frontal slices) of the tensors. As shown by [41], the natural convolution provided by the t-product between tensors opens a new direction of representing graph-based models, and the sketching developed for frontal dimensions allows more efficient computations over them.

It is of interest to explore the application of t-product in compressible tensor systems, for example, the butterfly compression in vector systems have been proven to scale up well [22,30,31] shows promising results for Kronecker tensor system, it remains to explore how tensor compressions work along with other kind of tensor products and associated systems.

## Acknowledgment

HL was supported by the Director, Office of Science, of the U.S. Department of Energy under Contract DE-AC02-05CH11231; U.S. National Science Foundation NSF-DMS 2412403. We also express our thanks to Dr. Yin-Ting Liao for earlier discussions in this work.

## References

- [1] Johann A Bengua, Ho N Phien, Hoang Duong Tuan, and Minh N Do. Efficient Tensor Completion for Color Image and Video Recovery: Low-rank Tensor Train. *IEEE Transactions on Image Processing*, 26(5):2466–2479, 2017.
- [2] Dimitri P Bertsekas. Incremental Gradient, Subgradient, and Proximal Methods for Convex Optimization: A Survey. *Optimization for Machine Learning*, page 85, 2011.
- [3] Xuan Bi, Xiwei Tang, Yubai Yuan, Yanqing Zhang, and Annie Qu. Tensors in Statistics. *Annual Review of Statistics and its Application*, 8:345–368, 2021.
- [4] Xuemei Chen and Jing Qin. Regularized Kaczmarz Algorithms for Tensor Recovery. *SIAM Journal on Imaging Sciences*, 14(4):1439–1471, 2021.
- [5] Yang Chen, Ziyang Luo, and Lingchen Kong. Low-rank Tensor Regression for Selection of Grouped Variables. *Journal of Multivariate Analysis*, page 105339, 2024.
- [6] Eric C Chi, Brian J Gaines, Will Wei Sun, Hua Zhou, and Jian Yang. Provable Convex Co-clustering of Tensors. *Journal of Machine Learning Research*, 21(214):1–58, 2020.
- [7] Eric C Chi and Tamara G Kolda. On tensors, sparsity, and nonnegative factorizations. *SIAM Journal on Matrix Analysis and Applications*, 33(4):1272–1299, 2012.
- [8] Younghyun Cho, James W Demmel, Michał Dereziński, Haoyun Li, Hengrui Luo, Michael W Mahoney, and Riley J Murray. Surrogate-based Autotuning for Randomized Sketching Algorithms in Regression Problems. *arXiv preprint arXiv:2308.15720*, 2023.
- [9] Western Electric Company. Finding his Voice, 1929.

- [10] Eisa Khosravi Dehdezi and Saeed Karimi. A Rapid and Powerful Iterative Method for Computing Inverses of Sparse Tensors with Applications. *Applied Mathematics and Computation*, 415:126720, 2022.
- [11] Kui Du and Xiao-Hui Sun. Randomized Regularized Extended Kaczmarz Algorithms for Tensor Recovery. *arXiv preprint arXiv:2112.08566*, 2021.
- [12] M El Guide, A El Ichi, K Jbilou, and FPA Beik. Tensor Krylov Subspace Methods via the Einstein Product with Applications to Image and Video Processing. *Applied Numerical Mathematics*, 181:347–363, 2022.
- [13] Jerome Friedman, Trevor Hastie, and Robert Tibshirani. Sparse Inverse Covariance Estimation with the Graphical LASSO. *Biostatistics*, 9(3):432–441, 2008.
- [14] Jerome H Friedman. Greedy Function Approximation: A Gradient Boosting Machine. *Annals of Statistics*, pages 1189–1232, 2001.
- [15] Mai Ghannam and Séverien Nkurunziza. Tensor Stein-rules in a Generalized Tensor Regression Model. *Journal of Multivariate Analysis*, 198:105206, 2023.
- [16] Robert M Gower, Denali Molitor, Jacob Moorman, and Deanna Needell. On Adaptive Sketch-and-project for Solving Linear Systems. *SIAM Journal on Matrix Analysis and Applications*, 42(2):954–989, 2021.
- [17] Robert M Gower and Peter Richtárik. Randomized Iterative Methods for Linear Systems. *SIAM Journal on Matrix Analysis and Applications*, 36(4):1660–1690, 2015.
- [18] Lars Grasedyck. Existence and Computation of Low Kronecker-rank Approximations for Large Linear Systems of Tensor Product Structure. *Computing*, 72:247–265, 2004.
- [19] Ning Hao, Misha E Kilmer, Karen Braman, and Randy C Hoover. Facial Recognition using Tensor-Tensor Decompositions. *SIAM Journal on Imaging Sciences*, 6(1):437–463, 2013.
- [20] Shiyuan He, Jianxin Yin, Hongzhe Li, and Xing Wang. Graphical Model Selection and Estimation for High-dimensional Tensor Data. *Journal of Multivariate Analysis*, 128:165–185, 2014.
- [21] Eric Kernfeld, Misha Kilmer, and Shuchin Aeron. Tensor-tensor Products with Invertible Linear Transforms. *Linear Algebra and its Applications*, 485:545–570, 2015.
- [22] Paul Michael Kielstra, Tianyi Shi, Hengrui Luo, Jianliang Qian, and Yang Liu. A Linear-Complexity Tensor Butterfly Algorithm for Compressing High-Dimensional Oscillatory Integral Operators. *ongoing*, pages 1–39, 2024+.
- [23] Misha E Kilmer and Carla D Martin. Factorization Strategies for Third-order Tensors. *Linear Algebra and its Applications*, 435(3):641–658, 2011.
- [24] Tamara G Kolda and Brett W Bader. Tensor Decompositions and Applications. *SIAM Review*, 51(3):455–500, 2009.
- [25] Tao Li, Qing-Wen Wang, and Xin-Fang Zhang. Gradient based Iterative Methods for Solving Symmetric Tensor Equations. *Numerical Linear Algebra with Applications*, 29(2):e2414, 2022.
- [26] Xingguo Li, Jarvis Haupt, and David Woodruff. Near Optimal Sketching of Low-rank Tensor Regression. *Advances in Neural Information Processing Systems*, 30, 2017.
- [27] Maolin Liang, Bing Zheng, and Ruijuan Zhao. Alternating Iterative Methods for Solving Tensor Equations with Applications. *Numerical Algorithms*, 80(4):1437–1465, 2019.
- [28] Cuiyu Liu, Chuanfu Xiao, Mingshuo Ding, and Chao Yang. Tensor-Based Sketching Method for the Low-Rank Approximation of Data Streams. *arXiv preprint arXiv:2209.14637*, 2022.
- [29] Shuangzhe Liu, Gotz Trenkler, et al. Hadamard, Khatri-Rao, Kronecker and other Matrix Products. *International Journal of Information and Systems Sciences*, 4(1):160–177, 2008.
- [30] Yang Liu, Pieter Ghysels, Lisa Claus, and Xiaoye Sherry Li. Sparse approximate multi-frontal factorization with butterfly compression for high-frequency wave equations. *SIAM Journal on Scientific Computing*, 43(5):S367–S391, 2021.

- [31] Yang Liu, Xin Xing, Han Guo, Eric Michielssen, Pieter Ghysels, and Xiaoye Sherry Li. Butterfly Factorization via Randomized Matrix-vector Multiplications. *SIAM Journal on Scientific Computing*, 43(2):A883–A907, 2021.
- [32] Wenqi Lu, Zhongyi Zhu, Rui Li, and Heng Lian. Statistical Performance of Quantile Tensor Regression with Convex Regularization. *Journal of Multivariate Analysis*, 200:105249, 2024.
- [33] Hengrui Luo, Akira Horiguchi, and Li Ma. Efficient Decision Trees for Tensor Regressions. *arXiv preprint arXiv:2408.01926*, 2024.
- [34] Hengrui Luo, Giovanni Nattino, and Matthew T. Pratola. Sparse Additive Gaussian Process Regression. *Journal of Machine Learning Research*, 23(61):1–34, 2022.
- [35] Rongke Lyu, Marina Vannucci, and Suprateek Kundu. Bayesian Tensor Modeling for Image-based Classification of Alzheimer’s Disease. *arXiv preprint arXiv:2312.08587*, 2023.
- [36] Anna Ma and Denali Molitor. Randomized Kaczmarz for Tensor Linear Systems. *BIT Numerical Mathematics*, 62(1):171–194, 2022.
- [37] Anna Ma, Deanna Needell, and Aaditya Ramdas. Convergence Properties of the Randomized Extended Gauss–Seidel and Kaczmarz Methods. *SIAM Journal on Matrix Analysis and Applications*, 36(4):1590–1604, 2015.
- [38] Carla D Martin, Richard Shafer, and Betsy LaRue. An Order-p Tensor Factorization with Applications in Imaging. *SIAM Journal on Scientific Computing*, 35(1):A474–A490, 2013.
- [39] Riley Murray, James Demmel, Michael W. Mahoney, N. Benjamin Erichson, Maksim Melnichenko, Osman Asif Malik, Laura Grigori, Michalánd Miles E. Lopes Dereziński, Tianyu Liang, Hengrui Luo, and Jack J. Dongarra. Randomized Numerical Linear Algebra: A Perspective on the Field with an Eye to Software. *arXiv preprint arXiv:2302.11474*, 2023.
- [40] Garvesh Raskutti and Michael W Mahoney. A Statistical Perspective on Randomized Sketching for Ordinary Least-squares. *Journal of Machine Learning Research*, 17(213):1–31, 2016.
- [41] Lothar Reichel and Ugochukwu O Ugwu. Tensor Arnoldi–Tikhonov and GMRES-type Methods for Ill-posed Problems with a t-product Structure. *Journal of Scientific Computing*, 90:1–39, 2022.
- [42] Nicholas D Sidiropoulos, Lieven De Lathauwer, Xiao Fu, Kejun Huang, Evangelos E Papalexakis, and Christos Faloutsos. Tensor Decomposition for Signal Processing and Machine Learning. *IEEE Transactions on Signal Processing*, 65(13):3551–3582, 2017.
- [43] Guangjing Song, Michael K. Ng, and Xiongjun Zhang. Robust Tensor Completion using Transformed Tensor Singular Value Decomposition. *Numerical Linear Algebra with Applications*, 27(3):e2299, 2020.
- [44] Ling Tang, Yanjun Zhang, and Hanyu Li. On Sketch-and-project Methods for Solving Tensor Equations. *arXiv preprint arXiv:2210.08241*, 2022.
- [45] Joel A Tropp, Alp Yurtsever, Madeleine Udell, and Volkan Cevher. Practical Sketching Algorithms for Low-rank Matrix Approximation. *SIAM Journal on Matrix Analysis and Applications*, 38(4):1454–1485, 2017.
- [46] Yining Wang, Hsiao-Yu Tung, Alexander J Smola, and Anima Anandkumar. Fast and Guaranteed Tensor Decomposition via Sketching. *Advances in Neural Information Processing Systems*, 28, 2015.
- [47] Leland Wilkinson and Hengrui Luo. A Distance-Preserving Matrix Sketch. *Journal of Computational and Graphical Statistics*, pages 1–15, 2022.

## A. Notation Conventions

We present the notations we used for different mathematical objects.

Definition	Notation
Left coefficient tensor	$\mathcal{A} \in \mathbb{R}^{n_1 \times n_2 \times n}$
Right coefficient tensor	$\mathcal{B} \in \mathbb{R}^{n_1 \times n_3 \times n}$
Solution tensor	$\mathcal{X} \in \mathbb{R}^{n_2 \times n_3 \times n}$
True solution tensor	$\mathcal{X}_* \in \mathbb{R}^{n_2 \times n_3 \times n}$
Row/column/frontal slice	$\mathcal{A}_{i::} = \mathcal{A}_i \in \mathbb{R}^{n_1 \times n_2 \times 1}$
Padded slice	$\tilde{\mathcal{A}}_i \in \mathbb{R}^{n_1 \times n_2 \times n}$
Solution tensor at iteration $t$	$\mathcal{X}(t)$
Residual tensor at iteration $t$	$\mathcal{R}(t)$
Error scalar at iteration $t$	$\mathcal{E}(t)$

## B. Proof of Theorem 8: frontal size $n = 2$

We first consider the case where  $n = 2$ .

*Proof.* In this case, the algorithm cycles through the 2 frontal slices one at a time, and the update in Algorithm 3.2 can then be simplified into the following cases:

Iteration  $t = 2k$ , the slice  $\tilde{\mathcal{A}}_2$  is chosen and we have

$$\mathcal{R}(2k) = \mathcal{B} - \tilde{\mathcal{A}}_1 * \mathcal{X}(2k-2) - \tilde{\mathcal{A}}_2 * \mathcal{X}(2k-1), \quad (\text{B.1})$$

$$\begin{aligned} \mathcal{X}(2k) &= \mathcal{X}(2k-1) + \alpha \tilde{\mathcal{A}}_2^T * \mathcal{R}(2k) \\ &= \left( \mathcal{I} - \alpha \tilde{\mathcal{A}}_2^T * \tilde{\mathcal{A}}_2 \right) * \mathcal{X}(2k-1) - \alpha \tilde{\mathcal{A}}_2^T * \tilde{\mathcal{A}}_1 * \mathcal{X}(2k-2) + \alpha \tilde{\mathcal{A}}_2^T * \mathcal{B}. \end{aligned} \quad (\text{B.2})$$

Iteration  $t = 2k+1$ , the slice  $\tilde{\mathcal{A}}_1$  is chosen and we obtain

$$\mathcal{R}(2k+1) = \mathcal{B} - \tilde{\mathcal{A}}_1 * \mathcal{X}(2k) - \tilde{\mathcal{A}}_2 * \mathcal{X}(2k-1) \quad (\text{B.3})$$

$$\begin{aligned} \mathcal{X}(2k+1) &= \mathcal{X}(2k) + \alpha \tilde{\mathcal{A}}_1^T * \mathcal{R}(2k+1) \\ &= \left( \mathcal{I} - \alpha \tilde{\mathcal{A}}_1^T * \tilde{\mathcal{A}}_1 \right) * \mathcal{X}(2k) - \alpha \tilde{\mathcal{A}}_1^T * \tilde{\mathcal{A}}_2 * \mathcal{X}(2k-1) + \alpha \tilde{\mathcal{A}}_1^T * \mathcal{B} \end{aligned} \quad (\text{B.4})$$

Let the (scalar) error between the current solution  $\mathcal{X}(k)$  and the actual solution  $\mathcal{X}_*$  at iteration  $k$  be  $\mathcal{E}(k) := \|\mathcal{X}(k) - \mathcal{X}_*\|$ . Recall  $\mathcal{X}_*$  satisfies  $(\tilde{\mathcal{A}}_1 + \tilde{\mathcal{A}}_2) * \mathcal{X}_* = \mathcal{A} * \mathcal{X}_* = \mathcal{B}$ . According to the two recursive relations in (B.2) and (B.4), we recognize that (B.2) can

be used to compute  $\mathcal{E}(2k)$

$$\begin{aligned}
\mathcal{E}(2k) &= \|\mathcal{X}(2k) - \mathcal{X}_*\| \\
&= \left\| \left( \mathcal{I} - \alpha \tilde{\mathcal{A}}_2^T * \tilde{\mathcal{A}}_2 \right) * \mathcal{X}(2k-1) - \alpha \tilde{\mathcal{A}}_2^T * \tilde{\mathcal{A}}_1 * \mathcal{X}(2k-2) + \alpha \tilde{\mathcal{A}}_2^T * \left( \tilde{\mathcal{A}}_1 + \tilde{\mathcal{A}}_2 \right) * \mathcal{X}_* - \mathcal{X}_* \right\| \\
&= \left\| \left( \mathcal{I} - \alpha \tilde{\mathcal{A}}_2^T * \tilde{\mathcal{A}}_2 \right) * \left( \mathcal{X}(2k-1) - \mathcal{X}_* \right) - \alpha \tilde{\mathcal{A}}_2^T * \tilde{\mathcal{A}}_1 \left( \mathcal{X}(2k-2) - \mathcal{X}_* \right) \right\| \\
&\leq \left\| \mathcal{I} - \alpha \tilde{\mathcal{A}}_2^T * \tilde{\mathcal{A}}_2 \right\|_{op} \|\mathcal{X}(2k-1) - \mathcal{X}_*\| + \left\| \alpha \tilde{\mathcal{A}}_2^T * \tilde{\mathcal{A}}_1 \right\|_{op} \|\mathcal{X}(2k-2) - \mathcal{X}_*\| \\
&= \left\| \mathcal{I} - \alpha \tilde{\mathcal{A}}_2^T * \tilde{\mathcal{A}}_2 \right\|_{op} \mathcal{E}(2k-1) + \left\| \alpha \tilde{\mathcal{A}}_2^T * \tilde{\mathcal{A}}_1 \right\|_{op} \mathcal{E}(2k-2), \tag{B.5}
\end{aligned}$$

and similarly we can use (B.4) for  $\mathcal{E}(2k+1)$ , to yield

$$\mathcal{E}(2k+1) \leq \left\| \mathcal{I} - \alpha \tilde{\mathcal{A}}_1^T * \tilde{\mathcal{A}}_1 \right\|_{op} \mathcal{E}(2k) + \left\| \alpha \tilde{\mathcal{A}}_1^T * \tilde{\mathcal{A}}_2 \right\|_{op} \mathcal{E}(2k-1). \tag{B.6}$$

Then we can combine (B.5) and (B.6) reduce to

$$\begin{aligned}
\mathcal{E}(2k) &\leq \left\| \mathcal{I} - \alpha \tilde{\mathcal{A}}_2^T * \tilde{\mathcal{A}}_2 \right\|_{op} \mathcal{E}(2k-1) + \left\| \alpha \tilde{\mathcal{A}}_2^T * \tilde{\mathcal{A}}_1 \right\|_{op} \mathcal{E}(2k-2), \\
\mathcal{E}(2k+1) &\leq \left\| \mathcal{I} - \alpha \tilde{\mathcal{A}}_1^T * \tilde{\mathcal{A}}_1 \right\|_{op} \mathcal{E}(2k) + \left\| \alpha \tilde{\mathcal{A}}_1^T * \tilde{\mathcal{A}}_2 \right\|_{op} \mathcal{E}(2k-1). \tag{B.7}
\end{aligned}$$

Now let  $\kappa_1 = \|\mathcal{I} - \alpha \tilde{\mathcal{A}}_1^T * \tilde{\mathcal{A}}_1\|_{op}$ ,  $\kappa_2 = \|\mathcal{I} - \alpha \tilde{\mathcal{A}}_2^T * \tilde{\mathcal{A}}_2\|_{op}$ , and  $\mu = \|\tilde{\mathcal{A}}_1^T * \tilde{\mathcal{A}}_2\|_{op}$ . We can pick  $\alpha$  so that  $\kappa_1, \kappa_2 < 1$ . Let the union bound of errors of the consecutive iterations  $\mathcal{M}_k := \max\{\|\mathcal{E}(2k-1)\|, \|\mathcal{E}(2k-2)\|\}$ . Then (B.5) and (B.6) reduce to

$$\begin{aligned}
\mathcal{E}(2k) &\leq \kappa_2 \mathcal{E}(2k-1) + \alpha \mu \mathcal{E}(2k-2), \\
&= (\kappa_2 + \alpha \mu) \mathcal{M}_k, \\
\mathcal{E}(2k+1) &\leq \kappa_1 \mathcal{E}(2k) + \alpha \mu \mathcal{E}(2k-1) \\
&\leq \kappa_1 (\kappa_2 + \alpha \mu) \mathcal{M}_k + \alpha \mu \mathcal{E}(2k-1) \\
&\leq (\kappa_1 \kappa_2 + (1 + \kappa_1) \alpha \mu) \mathcal{M}_k,
\end{aligned}$$

and thus,

$$\mathcal{M}_{k+1} \leq C \mathcal{M}_k,$$

where  $C = \max\{\kappa_2 + \alpha \mu, \kappa_1 \kappa_2 + (1 + \kappa_1) \alpha \mu\}$  and if  $\alpha < \min\left\{\frac{1-\kappa_2}{\mu}, \frac{1-\kappa_1 \kappa_2}{\mu(1+\kappa_2)}\right\}$  then  $C < 1$ . Namely, we proved the result.

**Remark 4.** From the above proof, we know that the convergence rate is controlled by the correlation  $\mu$  between slices defined by  $t$ -product, and the learning rate  $\alpha$ .

Note that if frontal slices are mutually orthogonal, e.g., if we have a diagonal tensor

$\mathcal{A}$ , then  $\mu = 0$  and

$$\begin{aligned}\mathcal{E}(2k) &\leq \kappa_2 \mathcal{E}(2k-1) \\ \mathcal{E}(2k+1) &\leq \kappa_1 \mathcal{E}(2k) \leq \kappa_1^k \kappa_2^k \mathcal{E}(0).\end{aligned}$$

Since  $\kappa_1, \kappa_2 < 1$ , this implies exponential convergence of Cyclic Slice Descent (Algorithm 3.2) in the form of  $\mathcal{E}(t) \leq \kappa^{t+1} \mathcal{E}(0)$  with factor  $\kappa$  where  $\kappa := \max_{j=1,2} \|\mathcal{I} - \alpha \tilde{\mathcal{A}}_j^T * \tilde{\mathcal{A}}_j\|_{op}$  for  $n = 2$ .

### C. Proof of Theorem 6

Following the idea of proof in Appendix B, we extend to the case where  $n > 2$  for Algorithm 3.2. We list the assumptions for our reference:

To prove Theorem 6, we will show that the upper bound on the approximation error decreases with every iteration. Lemma 10 provides a relationship between the current and previous  $n$  approximation errors. This is used in Lemma 11 to define the bounding coefficient. Lemma 12 shows that the bounding coefficient is decreasing. Before we prove these lemmas and the main theorem, we remind the reader of useful notation and assumptions in this section. In particular, we let

$$\begin{aligned}\kappa &= \max_{i=1,\dots,n} \|\mathcal{I} - \alpha \tilde{\mathcal{A}}_i^T * \tilde{\mathcal{A}}_i\|_{op}, \\ \mu &= \max_{\substack{i,j=1,\dots,n \\ i \neq j}} \|\tilde{\mathcal{A}}_i^T * \tilde{\mathcal{A}}_j\|_{op},\end{aligned}\tag{C.1}$$

and  $\|\cdot\|_{op}$  is the operator norm, defined as  $\|\mathcal{A}\|_{op} := \sup_{\|\mathcal{X}\|=1} \|\mathcal{A} * \mathcal{X}\|_2$ . We adopt the convention that  $\mathcal{X}(t) = 0$  when  $t < 0$  and thus,  $\mathcal{E}(t) = \|\mathcal{X}^*\|_F$  when  $t < 0$ .

**Assumption 1.** We assume the learning rate  $\alpha$  is chosen such that  $\kappa < 1$  and

$$\kappa + \alpha\mu(n-1) < 1.$$

**Lemma 10.** The approximation error at iteration  $t+1$  is bounded by a function of error from the previous  $n$  iterations:

$$\mathcal{E}(t+1) \leq \kappa \mathcal{E}(t) + \alpha\mu \sum_{i=1}^{n-1} \mathcal{E}(t-i).\tag{C.2}$$

*Proof.* Recall that the iteration step in Algorithm 3.2:

$$\mathcal{X}(t+1) = \mathcal{X}(t) + \alpha \tilde{\mathcal{A}}_{[t \pmod n]+1}^T * \mathcal{R}(t+1),$$

such that, since  $\mathcal{X}(t) = 0$  for  $t < 0$ , we can consider the last  $n$  iterated slices.

$$\begin{aligned}
\mathcal{R}(t+1) &= \mathcal{R}(t) - \tilde{\mathcal{A}}_i * \mathcal{X}(t) + \tilde{\mathcal{A}}_i * \mathcal{X}(t-n+1) \\
&= \mathcal{B} - \left( \tilde{\mathcal{A}}_{t \pmod{n}+1} * \mathcal{X}(t) + \tilde{\mathcal{A}}_{(t-1) \pmod{n}+1} * \mathcal{X}(t-1) + \right. \\
&\quad \left. \cdots + \tilde{\mathcal{A}}_{(t-n+1) \pmod{n}+1} * \mathcal{X}(t-n+1) \right) \\
&= \mathcal{B} - \sum_{i=0}^{n-1} \tilde{\mathcal{A}}_{[(t-i) \pmod{n}]+1} * \mathcal{X}(t-i) \\
&= \sum_{i=0}^{n-1} \tilde{\mathcal{A}}_{[(t-i) \pmod{n}]+1} * (\mathcal{X}_* - \mathcal{X}(t-i)). \tag{C.3}
\end{aligned}$$

The error  $\mathcal{E}(t+1)$  can be bounded as:

$$\begin{aligned}
\mathcal{E}(t+1) &= \|\mathcal{X}(t+1) - \mathcal{X}_*\|_F \\
&= \left\| \mathcal{X}(t) + \alpha \tilde{\mathcal{A}}_{[t \pmod{n}]+1}^T * \mathcal{R}(t+1) - \mathcal{X}_* \right\|_F \tag{C.4}
\end{aligned}$$

$$\begin{aligned}
&\leq \left\| \left( \mathcal{I} - \alpha \tilde{\mathcal{A}}_{[t \pmod{n}]+1}^T * \tilde{\mathcal{A}}_{[t \pmod{n}]+1} \right) * (\mathcal{X}(t) - \mathcal{X}_*) \right\|_F \\
&\quad + \left\| \alpha \tilde{\mathcal{A}}_{[t \pmod{n}]+1}^T * \left( \sum_{i=1}^{n-1} \tilde{\mathcal{A}}_{[(t-i) \pmod{n}]+1} * (\mathcal{X}_* - \mathcal{X}(t-i)) \right) \right\|_F \tag{C.5}
\end{aligned}$$

$$\begin{aligned}
&\leq \left\| \mathcal{I} - \alpha \tilde{\mathcal{A}}_{[t \pmod{n}]+1}^T * \tilde{\mathcal{A}}_{[t \pmod{n}]+1} \right\|_{op} \|\mathcal{X}_* - \mathcal{X}(t)\|_F \\
&\quad + \alpha \sum_{i=1}^{n-1} \left\| \tilde{\mathcal{A}}_{[t \pmod{n}]+1}^T * \tilde{\mathcal{A}}_{[(t-i) \pmod{n}]+1} \right\|_{op} \|\mathcal{X}_* - \mathcal{X}(t-i)\|_F \tag{C.6}
\end{aligned}$$

$$\begin{aligned}
&= \left\| \mathcal{I} - \alpha \tilde{\mathcal{A}}_{[t \pmod{n}]+1}^T * \tilde{\mathcal{A}}_{[t \pmod{n}]+1} \right\|_{op} \mathcal{E}(t) \\
&\quad + \alpha \sum_{i=1}^{n-1} \left\| \tilde{\mathcal{A}}_{[t \pmod{n}]+1}^T * \tilde{\mathcal{A}}_{[(t-i) \pmod{n}]+1} \right\|_{op} \mathcal{E}(t-i) \tag{C.7}
\end{aligned}$$

$$\leq \kappa \mathcal{E}(t) + \alpha \mu \sum_{i=1}^{n-1} \mathcal{E}(t-i), \tag{C.8}$$

where the first inequality follows from (C.3) and the triangle inequality, the second inequality follows from Remark 1, and then the last inequality uses the definitions of  $\kappa$  and  $\mu$ .

In (C.4) and (C.6), we have rather conservative bounds from these inequalities. Although there are scenarios where the equalities hold in these two inequalities, it is possible to improve these bounds.



**Lemma 11.** Define  $\epsilon_t \in \mathbb{R}$  as

$$\epsilon_t := \begin{cases} \kappa^t + \alpha\mu \sum_{j=0}^{t-1} \kappa^j \sum_{i=1}^{n-1} \epsilon_{t-1-j-i} & \text{if } t \geq 1 \\ 1 & \text{otherwise.} \end{cases} \quad (\text{C.9})$$

For all  $t \geq 1$ , the approximation error at iteration  $t$  is bounded above by:

$$\mathcal{E}(t) \leq \epsilon_t \mathcal{E}(0). \quad (\text{C.10})$$

*Proof.* When  $t \leq 0$

$$\mathcal{E}(t) = \|\mathcal{X}(t) - \mathcal{X}_*\| = \mathcal{E}(0),$$

since  $\mathcal{X}(t) = \mathcal{X}(0) = 0$  so  $\epsilon_t = 1$ . For  $t \geq 1$ , we proceed by induction. In the base case, we first consider  $t = 1$ . By (C.9), when  $t = 1$ :

$$\begin{aligned} \epsilon_1 &= \kappa^1 + \alpha\mu \sum_{j=0}^0 \kappa^j \sum_{i=1}^{n-1} \epsilon_{1-1-j-i} \\ &= \kappa + \alpha\mu \sum_{i=1}^{n-1} 1 = \kappa + \alpha\mu(n-1). \end{aligned}$$

On the other hand, by Lemma 10, we have

$$\begin{aligned} \mathcal{E}(1) &\leq \kappa \mathcal{E}(0) + \alpha\mu \sum_{i=1}^{n-1} \mathcal{E}(0-i) \\ &= (\kappa + \alpha\mu(n-1)) \mathcal{E}(0) = \epsilon_1 \mathcal{E}(0). \end{aligned}$$

where the equality follows from the convention that  $\mathcal{E}(i) = \mathcal{E}(0)$  for  $i < 0$ . Thus,  $\mathcal{E}(1) \leq \epsilon_1 \mathcal{E}(0)$ . Now let  $T \in \mathbb{N}$  and assume that for all  $t \leq T$ , (C.10) holds. Again, by Lemma 10, we have

$$\begin{aligned} \mathcal{E}(T+1) &\leq \kappa \mathcal{E}(T) + \alpha\mu \sum_{i=1}^{n-1} \mathcal{E}(T-i) \\ &\leq \left( \kappa \epsilon_T + \alpha\mu \sum_{i=1}^{n-1} \epsilon_{(T-i)} \right) \mathcal{E}(0), \end{aligned}$$

where the second inequality follows from our inductive hypothesis. Using the definition

of  $\epsilon_T$  and simplifying terms, we arrive at our desired conclusion:

$$\begin{aligned}
\mathcal{E}(T+1) &\leq \left( \kappa \epsilon_T + \alpha \mu \sum_{i=1}^{n-1} \epsilon_{(T-i)} \right) \mathcal{E}(0) \\
&= \left( \kappa \left( \kappa^T + \alpha \mu \sum_{j=0}^{T-1} \kappa^j \sum_{i=1}^{n-1} \epsilon_{T-1-j-i} \right) + \alpha \mu \sum_{i=1}^{n-1} \epsilon_{(T-i)} \right) \mathcal{E}(0) \\
&= \left( \kappa^{T+1} + \alpha \mu \sum_{j=0}^{T-1} \kappa^{j+1} \sum_{i=1}^{n-1} \epsilon_{T-1-j-i} + \alpha \mu \sum_{i=1}^{n-1} \epsilon_{(T-i)} \right) \mathcal{E}(0) \\
&= \left( \kappa^{T+1} + \alpha \mu \sum_{j=1}^T \kappa^j \sum_{i=1}^{n-1} \epsilon_{T-j-i} + \alpha \mu \cdot \kappa^0 \sum_{i=1}^{n-1} \epsilon_{(T-i)} \right) \mathcal{E}(0) \\
&= \left( \kappa^{T+1} + \alpha \mu \sum_{j=0}^T \kappa^j \sum_{i=1}^{n-1} \epsilon_{T-j-i} \right) \mathcal{E}(0) \\
&= \epsilon_{T+1} \mathcal{E}(0).
\end{aligned}$$

Note that we re-indexing in line 4 of the above sequence of arguments.

**Lemma 12.** *Let  $\epsilon_t$  be as defined in (C.9). For all  $t \geq 0$ ,  $\epsilon_{t+1} < \epsilon_t$ .*

*Proof.* We proceed by induction. For the base case, let  $t = 0$  then by definition

$$\epsilon_1 = (\kappa + \alpha \mu (n-1)) \epsilon_0 < \epsilon_0,$$

where the inequality follows from the second inequality  $\kappa + \alpha \mu (n-1) < 1$  of Assumption 1. Now let  $T \in \mathbb{N}$  and suppose for all  $t \leq T$ ,  $\epsilon_{t+1} < \epsilon_t$  holds. Then for  $\epsilon_{(T+1)+1}$ , we have

by definition of  $\epsilon_t$ :

$$\begin{aligned}
\epsilon_{(T+1)+1} &= \kappa^{(T+1)+1} + \alpha\mu \sum_{j=0}^{T+1} \kappa^j \sum_{i=1}^{n-1} \epsilon_{T+1-j-i} \\
&= \kappa^{(T+1)+1} + \alpha\mu \sum_{j=0}^T \kappa^j \sum_{i=1}^{n-1} \epsilon_{T+1-j-i} + \alpha\mu \kappa^{T+1} \sum_{i=1}^{n-1} \epsilon_{T+1-(T+1)-i} \\
&= \kappa^{(T+1)} (\kappa + \alpha\mu(n-1)) + \sum_{j=0}^T \kappa^j \sum_{i=1}^{n-1} \epsilon_{T+1-j-i} \\
&< \kappa^{(T+1)} (\kappa + \alpha\mu(n-1)) + \sum_{j=0}^T \kappa^j \sum_{i=1}^{n-1} \epsilon_{T-j-i} \\
&< \kappa^{(T+1)} + \alpha\mu \sum_{j=0}^T \kappa^j \sum_{i=1}^{n-1} \epsilon_{T-j-i} = \epsilon_{T+1},
\end{aligned}$$

where the first inequality follows from the inductive hypothesis and the second inequality follows from the second inequality  $\kappa + \alpha\mu < 1$  of Assumption 1.

*Proof.* (Proof of Theorem 6) Suppose that Assumption 1 holds. By Lemma 11, the approximation error at iteration  $t$  is  $\mathcal{E}(t) \leq \epsilon_t \mathcal{E}(0)$  and by Lemma 12,  $\epsilon_t \geq 0$  is decreasing. Since  $\mathcal{E}(t) \geq 0$  for all  $t$ , this implies that the approximation error is decreasing to zero.

## D. Proof of Theorem 9

Note that the proof of Theorem 6 relies on the system being consistent. In Lemma 10, we use the fact that  $\mathcal{B} = \mathcal{A} * \mathcal{X}^*$ . Now we assume that  $\mathcal{B} + \mathcal{B}_e = \mathcal{A} * \mathcal{X}^*$  where  $\mathcal{B}_e$  is the tensor error term. We still want to study  $\mathcal{R}(t) := \|\mathcal{B} - \mathcal{A} * \mathcal{X}(t)\|_F$  and the recursion is as follows:

$$\begin{aligned}
\mathcal{R}(t+1) &= \mathcal{R}(t) - \tilde{\mathcal{A}}_i * \mathcal{X}(t) + \tilde{\mathcal{A}}_i * \mathcal{X}(t-n+1) \\
&= \mathcal{B} - \mathcal{B}_e - \sum_{i=0}^{n-1} \tilde{\mathcal{A}}_{[(t-i) \bmod n]+1} * \mathcal{X}(t-i) \\
&= \sum_{i=0}^{n-1} \tilde{\mathcal{A}}_{[(t-i) \bmod n]+1} * (\mathcal{X}^* - \mathcal{X}(t-i)) - \mathcal{B}_e. \tag{D.1}
\end{aligned}$$

$$\begin{aligned}
\mathcal{E}(t+1) &= \|\mathcal{X}(t+1) - \mathcal{X}_*\|_F \\
&= \left\| \mathcal{X}(t) + \alpha \tilde{\mathcal{A}}_{[t \pmod n]+1}^T * \mathcal{R}(t+1) - \mathcal{X}_* \right\|_F \\
&\leq \left\| \left( \mathcal{I} - \alpha \tilde{\mathcal{A}}_{[t \pmod n]+1}^T * \tilde{\mathcal{A}}_{[t \pmod n]+1} \right) * (\mathcal{X}(t) - \mathcal{X}_*) \right\|_F \\
&\quad + \left\| \alpha \tilde{\mathcal{A}}_{[t \pmod n]+1}^T * \mathcal{B}_e \right\|_F \\
&\quad + \left\| \alpha \tilde{\mathcal{A}}_{[t \pmod n]+1}^T * \left( \sum_{i=1}^{n-1} \tilde{\mathcal{A}}_{[(t-i) \pmod n]+1} * (\mathcal{X}_* - \mathcal{X}(t-i)) \right) \right\|_F \tag{D.2}
\end{aligned}$$

$$\begin{aligned}
&\leq \left\| \mathcal{I} - \alpha \tilde{\mathcal{A}}_{[t \pmod n]+1}^T * \tilde{\mathcal{A}}_{[t \pmod n]+1} \right\|_{op} \|\mathcal{X}_* - \mathcal{X}(t)\|_F \\
&\quad + \left\| \alpha \tilde{\mathcal{A}}_{[t \pmod n]+1}^T * \mathcal{B}_e \right\|_F \tag{D.3}
\end{aligned}$$

$$\begin{aligned}
&\quad + \alpha \sum_{i=1}^{n-1} \left\| \tilde{\mathcal{A}}_{[t \pmod n]+1}^T * \tilde{\mathcal{A}}_{[(t-i) \pmod n]+1} \right\|_{op} \|\mathcal{X}_* - \mathcal{X}(t-i)\|_F \\
&= \left\| \mathcal{I} - \alpha \tilde{\mathcal{A}}_{[t \pmod n]+1}^T * \tilde{\mathcal{A}}_{[t \pmod n]+1} \right\|_{op} \mathcal{E}(t) + \alpha \left\| \tilde{\mathcal{A}}_{[t \pmod n]+1}^T * \mathcal{B}_e \right\|_F + \tag{D.4} \\
&\quad \alpha \sum_{i=1}^{n-1} \left\| \tilde{\mathcal{A}}_{[t \pmod n]+1}^T * \tilde{\mathcal{A}}_{[(t-i) \pmod n]+1} \right\|_{op} \mathcal{E}(t-i)
\end{aligned}$$

$$\begin{aligned}
&\leq \kappa \mathcal{E}(t) + \alpha \mu \sum_{i=1}^{n-1} \mathcal{E}(t-i) + \alpha \eta_e \tag{D.5}
\end{aligned}$$

where  $\eta_e := \max_{i=1, \dots, n} \left\| \tilde{\mathcal{A}}_i \right\|_{op} \|\mathcal{B}_e\|$ . Now consider the following definition and assumptions

$$\eta_t := \begin{cases} \kappa^t + \alpha\mu \sum_{j=0}^{t-1} \kappa^j \sum_{i=1}^{n-1} \epsilon_{t-1-j-i} + \frac{\alpha}{\mathcal{E}(0)} \eta_e = \epsilon_t + \frac{\alpha}{\mathcal{E}(0)} \eta_e & \text{if } t \geq 1 \\ 1 & \text{otherwise.} \end{cases} \quad (\text{D.6})$$

**Assumption 2.** We assume the learning rate  $\alpha$  is chosen such that  $\kappa < 1$  and

$$\kappa + \alpha\mu(n-1) + \frac{\alpha}{\mathcal{E}(0)} \eta_e < 1.$$

Then we repeat the arguments in Lemma 10 by supposing that

$$\begin{aligned} \mathcal{E}(T+1) &\leq \kappa \mathcal{E}(T) + \alpha\mu \sum_{i=1}^{n-1} \mathcal{E}(T-i) + \alpha\eta_e \\ &= \left( \kappa \epsilon_T + \alpha\mu \sum_{i=1}^{n-1} \epsilon_{T-i} + \frac{\alpha}{\mathcal{E}(0)} \eta_e \right) \mathcal{E}(0) \\ &= \left( \kappa \left( \kappa^T + \alpha\mu \sum_{j=0}^{T-1} \kappa^j \sum_{i=1}^{n-1} \epsilon_{T-1-j-i} \right) + \alpha\mu \sum_{i=1}^{n-1} \epsilon_{T-i} + \frac{\alpha}{\mathcal{E}(0)} \eta_e \right) \mathcal{E}(0) \\ &= \left( \kappa^{T+1} + \alpha\mu \sum_{j=1}^T \kappa^j \sum_{i=1}^{n-1} \epsilon_{T-j-i} + \alpha\mu \sum_{i=1}^{n-1} \epsilon_{T-i} + \frac{\alpha}{\mathcal{E}(0)} \eta_e \right) \mathcal{E}(0) \\ &= \left( \kappa^{T+1} + \alpha\mu \sum_{j=0}^T \kappa^j \sum_{i=1}^{n-1} \epsilon_{T-j-i} + \frac{\alpha}{\mathcal{E}(0)} \eta_e \right) \mathcal{E}(0) \\ &= \eta_{T+1} \mathcal{E}(0). \end{aligned}$$

And then  $\eta_{t+1} < \eta_t$  for  $t \geq 1$  follows from the same lines as Lemma 12: as long as  $\kappa + \alpha\mu(n-1) + \frac{\alpha}{\mathcal{E}(0)} \eta_e < 1$ , the line 5 of the below argument goes through:

$$\begin{aligned} \eta_{(T+1)+1} &= \epsilon_{T+1} + \frac{\alpha}{\mathcal{E}(0)} \eta_e \\ &= \kappa^{(T+1)+1} + \alpha\mu \sum_{j=0}^{T+1} \kappa^j \sum_{i=1}^{n-1} \epsilon_{T+1-j-i} + \frac{\alpha}{\mathcal{E}(0)} \eta_e \\ &= \kappa^{(T+1)+1} + \alpha\mu \sum_{j=0}^T \kappa^j \sum_{i=1}^{n-1} \epsilon_{T+1-j-i} + \alpha\mu \kappa^{T+1} \sum_{i=1}^{n-1} \epsilon_{T+1-(T+1)-i} + \frac{\alpha}{\mathcal{E}(0)} \eta_e \end{aligned}$$

$$\begin{aligned}
&= \kappa^{(T+1)} (\kappa + \alpha\mu(n-1)) + \sum_{j=0}^T \kappa^j \sum_{i=1}^{n-1} \epsilon_{T+1-j-i} + \frac{\alpha}{\mathcal{E}(0)} \eta_e \\
&< \kappa^{(T+1)} \left( \kappa + \alpha\mu(n-1) + \frac{\alpha}{\mathcal{E}(0)} \eta_e \right) + \sum_{j=0}^T \kappa^j \sum_{i=1}^{n-1} \epsilon_{T-j-i} + \frac{\alpha}{\mathcal{E}(0)} \eta_e \\
&< \kappa^{(T+1)} + \alpha\mu \sum_{j=0}^T \kappa^j \sum_{i=1}^{n-1} \epsilon_{T-j-i} + \frac{\alpha}{\mathcal{E}(0)} \eta_e = \epsilon_{T+1} + \frac{\alpha}{\mathcal{E}(0)} \eta_e = \eta_{T+1}.
\end{aligned}$$

### E. Corollary 7: blocked Case

Suppose that we still perform cyclic descent, but each time we consider a block of  $s$  consecutive slices. For simplicity we assume  $n/s$  is an integer, and this mean that we can write the residual as follows when we consider the last  $n/s$  iterated slices.

$$\begin{aligned}
&\mathcal{R}(t+1) \\
&= \mathcal{B} - \left( \tilde{\mathcal{A}}_{(t \bmod (n/s))}^s * \mathcal{X}(t) + \tilde{\mathcal{A}}_{(t-1 \bmod (n/s))}^s * \mathcal{X}(t-1) + \right. \\
&\quad \left. \cdots + \tilde{\mathcal{A}}_{(t-n/s \bmod (n/s))}^s * \mathcal{X}(t-T+1) \right), \\
&= \mathcal{B} - \sum_{i=0}^{n/s-1} \tilde{\mathcal{A}}_{(t-i)}^s * \mathcal{X}(t-i) \\
&= \sum_{i=0}^{n/s-1} \tilde{\mathcal{A}}_{(t-i)}^s * (\mathcal{X}_* - \mathcal{X}(t-i)). \tag{E.1}
\end{aligned}$$

We define  $\tilde{\mathcal{A}}_i^s := \tilde{\mathcal{A}}_{i.(s-1)+1} + \tilde{\mathcal{A}}_{i.(s-1)+2} + \cdots + \tilde{\mathcal{A}}_{i.s}$  to be the sum of  $s$  padded slices. And the same lines of arguments in (C.3) still hold with  $T = n/s$  in (E.1):

$$\begin{aligned}
\mathcal{E}(t+1) &\leq \kappa(s)\mathcal{E}(t) + \alpha\mu \sum_{i=1}^{n/s-1} \mathcal{E}(t-i) \tag{E.2} \\
&\leq \kappa(s)^t \mathcal{E}(0) + \alpha\mu(s) \sum_{j=0}^t \sum_{i=1}^{n/s} \kappa(s)^j \mathcal{E}(t-j-i),
\end{aligned}$$

where we need new constants  $\kappa(s), \mu(s)$  depending on the block size  $s$ , defined with respect to each block (when  $s = 1$  these reduces to (C.1))

$$\begin{aligned}
\kappa(s) &= \max_{i=1, \dots, n/s} \|\mathcal{I} - \alpha \tilde{\mathcal{A}}_i^{sT} * \tilde{\mathcal{A}}_i^s\|_{op}, \tag{E.3} \\
\mu(s) &= \max_{\substack{i, j=1, \dots, n/s \\ i \neq j}} \|\tilde{\mathcal{A}}_i^{sT} * \tilde{\mathcal{A}}_j^s\|_{op}.
\end{aligned}$$

And the analog of the equation (C.9) can be written as follows, where the contraction factor  $\epsilon_t(s)$  depends on the block size  $s$ :

$$\epsilon_t(s) := \begin{cases} \kappa(s)^t + \alpha\mu(s) \sum_{j=0}^{t-1} \kappa^j(s) \sum_{i=1}^{n-1} \epsilon_{t-1-j-i}(s) & \text{if } t \geq 1 \\ 1 & \text{otherwise.} \end{cases} \quad (\text{E.4})$$

The verification for  $t \leq n/s$  as the induction base case. That means, our assumption needs to depend on the block size  $s$  as well:

**Assumption 3.** *We assume the learning rate  $\alpha$  is chosen such that  $\kappa(s) < 1$  and*

$$\kappa(s) + \alpha\mu(s)(n/s - 1) < 1.$$

To interpret this, it is not hard to observe that  $\kappa(s) \leq \kappa_1$  where  $\kappa_1$  is computed with a different  $\alpha_1 = \alpha/s^4$  since for  $i = 1, \dots, n/s$

$$\begin{aligned} \|\mathcal{I} - \alpha \tilde{\mathcal{A}}_i^{sT} * \tilde{\mathcal{A}}_i^s\|_{op} &= \left\| \mathcal{I} - \alpha \left( \tilde{\mathcal{A}}_{i \cdot (s-1)+1} + \tilde{\mathcal{A}}_{i \cdot (s-1)+2} + \dots + \tilde{\mathcal{A}}_{i \cdot s} \right)^T * \right. \\ &\quad \left. \left( \tilde{\mathcal{A}}_{i \cdot (s-1)+1} + \tilde{\mathcal{A}}_{i \cdot (s-1)+2} + \dots + \tilde{\mathcal{A}}_{i \cdot s} \right) \right\|_{op} \\ &= \left\| \mathcal{I} - \alpha \sum_{i_1, i_2 = i \cdot (s-1)+1, \dots, i \cdot s} \tilde{\mathcal{A}}_{i_1}^T * \tilde{\mathcal{A}}_{i_2} \right\|_{op} \\ &\geq \left| \|\mathcal{I}\|_{op} - \alpha \left\| \sum_{i_1, i_2 = i \cdot (s-1)+1, \dots, i \cdot s} \tilde{\mathcal{A}}_{i_1}^T * \tilde{\mathcal{A}}_{i_2} \right\|_{op} \right| \\ &\geq \left| \|\mathcal{I}\|_{op} - s^2 \alpha \max_{i=1, \dots, n} \left\| \tilde{\mathcal{A}}_i^T * \tilde{\mathcal{A}}_i \right\|_{op} \right| \end{aligned}$$

The  $\mu(s) \leq s^2 \mu$  holds with a similar calculation.

$$\begin{aligned} \|\tilde{\mathcal{A}}_i^{sT} * \tilde{\mathcal{A}}_j^s\|_{op} &= \left\| \left( \tilde{\mathcal{A}}_{i \cdot (s-1)+1} + \tilde{\mathcal{A}}_{i \cdot (s-1)+2} + \dots + \tilde{\mathcal{A}}_{i \cdot s} \right)^T * \left( \tilde{\mathcal{A}}_{j \cdot (s-1)+1} + \tilde{\mathcal{A}}_{j \cdot (s-1)+2} + \dots + \tilde{\mathcal{A}}_{j \cdot s} \right) \right\|_{op} \\ &= \left\| \sum_{\substack{i_1 = i \cdot (s-1) + 1, \dots, i \cdot s \\ i_2 = j \cdot (s-1) + 1, \dots, j \cdot s}} \tilde{\mathcal{A}}_{i_1}^T * \tilde{\mathcal{A}}_{i_2} \right\|_{op} \\ &\leq s^2 \max_{i \neq j, i, j = 1, \dots, n} \left\| \tilde{\mathcal{A}}_i^T * \tilde{\mathcal{A}}_j \right\|_{op}. \end{aligned}$$

These calculation shows that

$$\kappa(s) + \alpha\mu(s)(n/s - 1) \leq \kappa_1 + \alpha s^2 \mu(n/s - 1).$$

And the Assumption 3 becomes more restrictive for larger block size  $s$ . In practice these are a smaller set ( $n/s < n$ ) of conditions compared to assumptions in Theorem 6.

Analogous to the argument in Theorem 6, via (E.2) we have that:

$$\begin{aligned}
\mathcal{E}(t+1) &= \|\mathcal{X}(t+1) - \mathcal{X}_*\|_F \\
&= \left\| \mathcal{X}(t) + \alpha \tilde{\mathcal{A}}_{[t \pmod{n)]+1}^T * \mathcal{R}(t+1) - \mathcal{X}_* \right\|_F \\
&\leq \left\| \left( \mathcal{I} - \alpha \tilde{\mathcal{A}}_{[t \pmod{n)]+1}^T * \tilde{\mathcal{A}}_{[t \pmod{n)]+1} \right) * (\mathcal{X}(t) - \mathcal{X}_*) \right\|_F \\
&\quad + \left\| \alpha \tilde{\mathcal{A}}_{[t \pmod{n)]+1}^T * \left( \sum_{i=1}^{n-1} \tilde{\mathcal{A}}_{[(t-i) \pmod{n)]+1} * (\mathcal{X}_* - \mathcal{X}(t-i)) \right) \right\|_F \\
&\leq \left\| \mathcal{I} - \alpha \tilde{\mathcal{A}}_{[t \pmod{n)]+1}^T * \tilde{\mathcal{A}}_{[t \pmod{n)]+1} \right\|_{op} \|\mathcal{X}_* - \mathcal{X}(t)\|_F \\
&\quad + \alpha \sum_{i=1}^{n-1} \left\| \tilde{\mathcal{A}}_{[t \pmod{n)]+1}^T * \tilde{\mathcal{A}}_{[(t-i) \pmod{n)]+1} \right\|_{op} \|\mathcal{X}_* - \mathcal{X}(t-i)\|_F \\
&= \left\| \mathcal{I} - \alpha \tilde{\mathcal{A}}_{[t \pmod{n)]+1}^T * \tilde{\mathcal{A}}_{[t \pmod{n)]+1} \right\|_{op} \mathcal{E}(t) \\
&\quad + \alpha \sum_{i=1}^{n-1} \left\| \tilde{\mathcal{A}}_{[t \pmod{n)]+1}^T * \tilde{\mathcal{A}}_{[(t-i) \pmod{n)]+1} \right\|_{op} \mathcal{E}(t-i) \\
&\leq \kappa \mathcal{E}(t) + \alpha \mu \sum_{i=1}^{n-1} \mathcal{E}(t-i), \tag{E.5}
\end{aligned}$$

$$\begin{aligned}
\mathcal{E}(t+1) &\leq \kappa(s)^t \epsilon_T(s) + \alpha \mu(s) \sum_{j=0}^t \sum_{i=1}^{n/s} \kappa(s)^j \mathcal{E}(t-j-i), \\
&= \|\mathcal{X}(t+1) - \mathcal{X}_*\|_F \\
&= \left\| \mathcal{X}(t) + \alpha \tilde{\mathcal{A}}_{[t \pmod{n/s)]+1}^{sT} * \mathcal{R}(t+1) - \mathcal{X}_* \right\|_F \\
&\leq \left\| \left( \mathcal{I} - \alpha \tilde{\mathcal{A}}_{[t \pmod{n/s)]+1}^{sT} * \tilde{\mathcal{A}}_{[t \pmod{n/s)]+1}^s \right) * (\mathcal{X}(t) - \mathcal{X}_*) \right\|_F \\
&\quad + \left\| \alpha \tilde{\mathcal{A}}_{[t \pmod{n/s)]+1}^{sT} * \left( \sum_{i=1}^{n/s-1} \tilde{\mathcal{A}}_{[(t-i) \pmod{n/s)]+1} * (\mathcal{X}_* - \mathcal{X}(t-i)) \right) \right\|_F \\
&\leq \left\| \mathcal{I} - \alpha \tilde{\mathcal{A}}_{[t \pmod{n/s)]+1}^{sT} * \tilde{\mathcal{A}}_{[t \pmod{n/s)]+1}^s \right\|_{op} \|\mathcal{X}_* - \mathcal{X}(t)\|_F
\end{aligned}$$



$$\begin{aligned}
& + \alpha \sum_{i=1}^{n/s-1} \left\| \tilde{\mathcal{A}}^{sT}_{[t \pmod{n/s]+1]} * \tilde{\mathcal{A}}^s_{[(t-i) \pmod{n/s]+1]} \right\|_{op} \|(\mathcal{X}_* - \mathcal{X}(t-i))\|_F \\
& = \left\| \mathcal{I} - \alpha \tilde{\mathcal{A}}^{sT}_{[t \pmod{n/s]+1]} * \tilde{\mathcal{A}}^s_{[t \pmod{n/s]+1]} \right\|_{op} \mathcal{E}(t) + \\
& \alpha \sum_{i=1}^{n/s-1} \left\| \tilde{\mathcal{A}}^{sT}_{[t \pmod{n/s]+1]} * \tilde{\mathcal{A}}^s_{[(t-i) \pmod{n/s]+1]} \right\|_{op} \mathcal{E}(t-i) \\
& \leq \kappa(s) \mathcal{E}(t) + \alpha \mu(s) \sum_{i=1}^{n/s} \mathcal{E}(t-i) \leq \dots \\
& \leq \left( \kappa(s)^{t+1} + \alpha \mu(s) \sum_{j=0}^t \kappa(s)^j \sum_{i=1}^{n/s-1} \epsilon_{t-j-i}(s) \right) \mathcal{E}(0) \\
& = \epsilon_{T+1}(s) \mathcal{E}(0).
\end{aligned}$$

With the Assumption, we can show

$$\begin{aligned}
\epsilon_{(T+1)+1}(s) & = \kappa^{(T+1)+1}(s) + \alpha \mu(s) \sum_{j=0}^{T+1} \kappa(s)^j \sum_{i=1}^{n/s-1} \epsilon_{T+1-j-i}(s) \\
& = \kappa^{(T+1)+1}(s) + \alpha \mu(s) \sum_{j=0}^T \kappa(s)^j \sum_{i=1}^{n/s-1} \epsilon_{T+1-j-i}(s) + \alpha \mu(s) \kappa(s)^{T+1} \sum_{i=1}^{n/s-1} \epsilon_{T+1-(T+1)-i}(s) \\
& = \kappa^{(T+1)}(s) (\kappa(s) + \alpha \mu(s) \cdot (n/s - 1)) + \sum_{j=0}^T \kappa(s)^j \sum_{i=1}^{n/s-1} \epsilon_{T+1-j-i}(s) \\
& < \kappa^{(T+1)}(s) (\kappa(s) + \alpha \mu(s) \cdot (n/s - 1)) + \sum_{j=0}^T \kappa(s)^j \sum_{i=1}^{n/s-1} \epsilon_{T-j-i}(s) \\
& < \kappa^{(T+1)}(s) + \alpha \mu(s) \cdot \sum_{j=0}^T \kappa(s)^j \sum_{i=1}^{n/s-1} \epsilon_{T-j-i}(s) = \epsilon_{T+1}(s).
\end{aligned}$$

This also allows us to discuss a special case, where the block size  $s = n$ , and the Algorithm 3.2 reduces to full gradient descent for (1.1). Then, our Assumption 3 becomes this only sufficient condition  $\kappa < 1$ , which means that unless all slices are orthogonal under t-product, the full gradient descent should converge.